

JAERI - M  
87-204

FAST WAVE CURRENT-DRIVE IN INTOR PLASMA

December 1987

Yasuaki KISHIMOTO, Tomonori TAKIZUKA, Kiyotaka HAMAMATSU  
Atsushi FUKUYAMA\*, Sanae ITOH\*\* and Kimitaka ITOH\*\*\*

JAERI-Mレポートは、日本原子力研究所が不定期に公刊している研究報告書です。  
入手の間合わせは、日本原子力研究所技術情報部情報資料課（〒319-11茨城県那珂郡東海村）あて、お申しこしください。なお、このほかに財団法人原子力弘済会資料センター（〒319-11 茨城県那珂郡東海村日本原子力研究所内）で複写による実費頒布をおこなっております。

JAERI-M reports are issued irregularly.

Inquiries about availability of the reports should be addressed to Information Division  
Department of Technical Information, Japan Atomic Energy Research Institute, Tokai-mura, Naka-gun, Ibaraki-ken 319-11, Japan.

©Japan Atomic Energy Research Institute, 1987

---

編集兼発行	日本原子力研究所
印刷	いばらき印刷㈱

FAST WAVE CURRENT-DRIVE IN INTOR PLASMA

Yasuaki KISHIMOTO, Tomonori TAKIZUKA, Kiyotaka HAMAMATSU<sup>+</sup>  
Atsushi FUKUYAMA\*, Sanae ITOH\*\* and Kimitaka ITOH\*\*\*

Department of Thermonuclear Fusion Research  
Naka Fusion Research Establishment  
Japan Atomic Energy Research Institute  
Naka-machi, Naka-gun, Ibaraki-ken

(Received November 26, 1987)

The global analysis of the fast wave current-drive in INTOR plasma considering the entire antenna-plasma system is presented. The phase shifted antenna array is used to inject the wave momentum to the plasma. The accessibility condition of the fast wave is investigated in order to optimize the launching condition. The optimum phase for the efficient current-drive is found and the global efficiency about  $(0.15 \sim 0.18)A/W$  is obtained in the density and temperature region of  $\bar{n}_e \approx 7 \times 10^{19} m^{-3}$  and  $\bar{T}_e \approx 20$  keV. The value of the fusion energy multiplication factor is estimated when the plasma current is sustained by the RF wave. It is found that the higher temperature and lower density plasma is more efficient for a tokamak reactor under the condition of the constant plasma pressure. The spatial profile of the induced current is also obtained and shows the possibility of the current profile control by changing the antenna phase.

Keywords: Current-Drive, Fast Wave, Antenna Design, Tokamak Reactor  
Current-Drive Efficiency, Accessibility Condition, Q value,  
Fusion Energy Multiplication

---

+ Department of Large Tokamak Research

\* School of Engineering, Okayama University

\*\* Institute for Fusion Theory, Hiroshima University

\*\*\* Plasma Physics Laboratory, Kyoto University

# INTOR プラズマに於ける速波電流駆動

日本原子力研究所那珂研究所核融合研究部

岸本泰明・滝塚知典・浜松清隆<sup>+</sup>

福山 淳<sup>\*</sup>・伊藤早苗<sup>\*\*</sup>・伊藤公孝<sup>\*\*\*</sup>

(1987年11月26日受理)

INTOR プラズマにおける速波電流駆動がアンテナープラズマ全系を考慮して巨視的に解析された。位相差を有するアンテナ列が波の運動量をプラズマに与えるため用いられている。波の放射条件を最適化するために速波の近接条件が調べられた。効率の良い電流駆動を与える最適なアンテナ位相が見つかり、 $\bar{n}_e \simeq 7 \times 10^{19} \text{ m}^{-3}$  及び  $T_e \simeq 20 \text{ keV}$  の密度と温度領域において (0.15 ~ 0.18) A/W 程度の総合効率が得られた。プラズマ電流が高周波によって支えられている場合の核融合反応のエネルギー増倍率の値が評価されている。プラズマ圧力一定の条件下ではより高温かつ低密度のプラズマが、トカマクによる核融合炉を考える上ではより有効であることが明らかになった。また駆動電流の空間分布も得られており、アンテナの位相変化による電流分布制御の可能性も示されている。

---

那珂研究所 : 〒311-02 茨城県那珂郡那珂町大字向山 801-1

+ 臨界プラズマ研究部

\* 岡山大学工学部

\*\* 広島大学核融合理論研究センター

\*\*\* 京都大学ヘリオトロン核融合研究センター

## Contents

1. Introduction .....	1
2. Plasma model and basic equations .....	2
2.1 Plasma model and wave equation .....	2
2.2 Velocity diffusion .....	4
2.3 Current by bulk electrons .....	5
2.4 Current-drive efficiency .....	7
3. Antenna design .....	8
3.1 Accessibility condition .....	8
3.2 Phase shifted antenna array .....	10
4. Numerical Results and analysis .....	12
4.1 Phase dependence .....	12
4.2 Plasma parameter dependence .....	15
4.3 Performance of tokamak reactor .....	16
5. Concluding remarks .....	18
Acknowledgements .....	19
Reference .....	20

## 目 次

1. 序 論 .....	1
2. プラズマモデルと基礎方程式 .....	2
2.1 プラズマモデルと波動方程式 .....	2
2.2 速度拡散 .....	4
2.3 バルク電子による電流 .....	5
2.4 電流駆動効率 .....	7
3. アンテナ設計 .....	8
3.1 近接条件 .....	8
3.2 位相差を有するアンテナ列 .....	10
4. 数値結果と解析 .....	12
4.1 位相依存性 .....	12
4.2 プラズマパラメーター依存性 .....	15
4.3 トカマク炉としての性能 .....	16
5. 結 論 .....	18
謝 辞 .....	19
参考文献 .....	20

## 1. Introduction

The continuous sustainment of the plasma current is one of the most important problems for a tokamak reactor. The lower-hybrid-wave current-drive has been obtained several promising results in the relatively lower density plasma regime[1-5]. Several experiments, however, show the density limit depending on the wave frequency[6,7]. Recently, the RF current-drive by using the fast wave is expected for the high density plasma because the restriction for the density limit is considered to be weak compared with the lower-hybrid wave[8-12]. In the case of the fast wave, the polarization of the parallel electric field, which induces the DC current, is smaller than that of the slow wave. Then, the fast wave may easily penetrate into the plasma center and deposit the energy and momentum without being absorbed in the peripheral region.

In the previous paper[13], we presented the global analysis of the ICRF current-drive by using the mode-converted ion Bernstein wave in the medium-size tokamak. The complete antenna-plasma system is introduced and the wave-propagation is analysed with the Fokker-Planck calculation. We examined the antenna phase dependence of the induced current by changing the launching condition and estimated the global current-drive efficiency (the ratio of the total induced current to the total emitted power) as well as the radial profile of the induced DC current.

In this article, we investigate the fast wave current-drive in the high density and high temperature plasma to simulate the reactor-size tokamak, such as INTOR. In order to maximize the current-drive efficiency, we present the guideline of the antenna design by use of the phase shifted antenna array. We first investigate the accessibility condition of the fast wave, and determine the optimum launching condition such as the spacing between two adjacent antennas and the total antenna number. Then, we study the phase dependence and the plasma parameter dependence of the induced current. The center-peaked current profile is obtained around the optimum antenna phase and the global current-drive efficiency reaches the value around  $0.075\text{A/W}$  within the framework of the 1-dimensional treatment of the Fokker-Planck equation in the velocity space. We also investigate the performance of the fast wave current-driven tokamak reactor by examining the fusion energy multiplication factor,  $Q$ . It is found that the higher temperature and lower density plasma is more efficient for a tokamak reactor under the condition of the constant plasma pressure when the plasma

current is sustained by the RF-wave. The plan of this paper is as follows. In section 2, we examine the accessibility condition of the fast wave and present the guideline of the antenna design. The antenna phase dependence and the plasma parameter dependence are examined in section 4. The  $Q$  value is also estimated in this section. In the final section, the results are summarized and discussed.

## 2. Plasma model and basic equations

In this section, we briefly survey the plasma model and basic equations for the wave-propagation according to Ref.13. The electron velocity diffusion due to the wave field and Coulomb collisions is described in subsection 2-2. The additional current produced by nonresonant bulk electrons is estimated in subsection 2-3. In subsection 2-4, the formula of the current-drive efficiency obtained in subsections 2-2 and 2-3 is examined compared with the another model.

### 2.1 Plasma model and wave equation

We consider the propagation of the fast wave in a slab plasma immersed in the strong magnetic field along the  $z$ -direction. The magnitude of the magnetic field varies in the  $x$ -direction as  $B(x)=B_0/(1+x/R_0)$ , where  $R_0$  is the major radius. The effect of the poloidal field is neglected for simplicity. The density and temperature are assumed to vary in the  $x$ -direction taking the parabolic profiles;

$$n(x)=(n_0-n_b)\left(1-\frac{x^2}{a^2}\right)+n_b, \quad (1)$$

$$T(x)=(T_0-T_b)\left(1-\frac{x^2}{a^2}\right)+T_b, \quad (2)$$

where the subscript 0 represents the central value and the subscript b denotes the value at the plasma boundary( $x=\pm a$ ).

The model antenna, which carries the sheet current in the  $y$ -direction, is placed at  $x=d$  in the low-field-side(LFS). Since the plasma parameters are independent of  $z$ , the  $z$ -profile of the antenna current,  $J_y^A(z)$ , is Fourier-decomposed as



current is sustained by the RF-wave. The plan of this paper is as follows. In section 2, we examine the accessibility condition of the fast wave and present the guideline of the antenna design. The antenna phase dependence and the plasma parameter dependence are examined in section 4. The  $Q$  value is also estimated in this section. In the final section, the results are summarized and discussed.

## 2. Plasma model and basic equations

In this section, we briefly survey the plasma model and basic equations for the wave-propagation according to Ref.13. The electron velocity diffusion due to the wave field and Coulomb collisions is described in subsection 2-2. The additional current produced by nonresonant bulk electrons is estimated in subsection 2-3. In subsection 2-4, the formula of the current-drive efficiency obtained in subsections 2-2 and 2-3 is examined compared with the another model.

### 2.1 Plasma model and wave equation

We consider the propagation of the fast wave in a slab plasma immersed in the strong magnetic field along the  $z$ -direction. The magnitude of the magnetic field varies in the  $x$ -direction as  $B(x)=B_0/(1+x/R_0)$ , where  $R_0$  is the major radius. The effect of the poloidal field is neglected for simplicity. The density and temperature are assumed to vary in the  $x$ -direction taking the parabolic profiles;

$$n(x)=(n_0-n_b)\left(1-\frac{x^2}{a^2}\right)+n_b, \quad (1)$$

$$T(x)=(T_0-T_b)\left(1-\frac{x^2}{a^2}\right)+T_b, \quad (2)$$

where the subscript 0 represents the central value and the subscript b denotes the value at the plasma boundary( $x=\pm a$ ).

The model antenna, which carries the sheet current in the  $y$ -direction, is placed at  $x=d$  in the low-field-side(LFS). Since the plasma parameters are independent of  $z$ , the  $z$ -profile of the antenna current,  $J_y^A(z)$ , is Fourier-decomposed as

$$J_y^A = \sum_{k_n} \hat{J}(k_n) \delta(x-d) \exp(ik_n z - i\omega t), \quad (3)$$

where  $k_n = n/R_0$  is the toroidal wave number. The wave electric field is described by the following wave equation,

$$\nabla \times \nabla \times \vec{E} - \frac{\omega^2}{c^2} \vec{E} - i\omega\mu_0 \left( \sum_s \vec{J}_s + \vec{J}^A \right) = 0. \quad (4)$$

The oscillating current carried by the plasma species  $s$  (electron and ions),  $\vec{J}_s$ , is derived from the non-local expression for the induced current ;

$$\vec{J}_s(\vec{r}) = \int \vec{\sigma}_s[\vec{r} - \vec{r}', (\vec{r} + \vec{r}')/2] \vec{E}(\vec{r}') d\vec{r}',$$

by assuming that the characteristic length of the inhomogeneity of the equilibrium is small compared to the gyro-radius,  $\rho$ , and retaining the second order with respect to  $k_\perp \rho$  ( $k_\perp$  ; wave number perpendicular to the magnetic field). The conductivity tensor,  $\vec{\sigma}_s$ , is calculated by the kinetic treatment in the collisionless limit. The explicit form of  $\vec{J}_s$  is given in Ref.14. The ion cyclotron dampings of the higher harmonics,  $\omega \geq 3\omega_{ci}$ , are not included in the conductivity tensor,  $\vec{\sigma}_s$ . Since we choose rather higher frequency fast wave around  $\omega \geq 6\omega_{ci}$ , the ion cyclotron damping is negligible and the wave propagation is unchanged by the neglect of this damping. In the numerical calculation, Eq.(4) is Fourier decomposed in the  $z$ -direction and the wave electric field is solved for each Fourier component,  $\vec{E}_{k_n}(x) = (E_{xn}, E_{yn}, E_{zn})$ , by employing the method of the multi-layer division in the  $x$ -direction, which is bounded by the conductive shells at  $x = \pm b$ .

Since we are retaining up to the second order with respect to  $k_\perp \rho_e$  ( $\rho_e$  ; electron Larmor radius) in  $\vec{J}_e$ , the electron power absorption includes not only the Landau damping but also the contributions from the transit time magnetic pumping(TTMP) and the cross term between  $E_y$  and  $E_z$ . When the input power is small and the deformation of the electron distribution function from the Maxwellian is negligible, the electron power absorption is given by,

$$P_e = \frac{1}{2} R_e \left\{ E_z^* \sigma_{eHzz}^{(0)} \left( E_z + \frac{1}{2} \frac{\partial^2 E_z}{\partial x^2} \right) - \frac{1}{2} E_y^* \sigma_{eHyx}^{(2)} \frac{\partial^2 E_y}{\partial x^2} - i \left( E_z^* \sigma_{eHzx}^{(1)} \frac{\partial E_y}{\partial x} + E_y^* \sigma_{eHyx}^{(1)} \frac{\partial E_z}{\partial x} \right) \right\} \quad (5)$$

where  $\tilde{\sigma}_{eH}$  denotes the Hermitian part of  $\tilde{\sigma}_e$  and  $\tilde{\sigma}_{eH}^{(0)} = [\tilde{\sigma}_{eH}]_{k_x=0}$ ,  $\tilde{\sigma}_{eH}^{(1)} = [\partial \tilde{\sigma}_{eH} / \partial k_x]_{k_x=0}$  and  $\tilde{\sigma}_{eH}^{(2)} = [\partial^2 \tilde{\sigma}_{eH} / \partial k_x^2]_{k_x=0}$ . Here, subscripts  $\alpha$  and  $\beta$  stand for  $x, y$  and  $z$  and the symbol  $*$  represents the complex conjugate. The power loss to the walls per unit antenna length in the  $y$ -direction,  $\bar{P}_w$ , is given by

$$\bar{P}_w = \frac{\pi R_0}{\mu_0 \omega} \left\{ \left| \text{Im} \left( E_y^* \frac{\partial E_y}{\partial x} \right)_{x=-b} \right| + \left| \text{Im} \left( E_y^* \frac{\partial E_y}{\partial x} \right)_{x=b} \right| \right\}, \quad (6)$$

and the total power input per unit antenna length in the  $y$ -direction,  $\bar{P}_A$ , is defined by

$$\bar{P}_A = 2\pi R_0 \int_{-a}^a P_e(x) dx + \bar{P}_w. \quad (7)$$

Note that Eqs.(5)-(7) are also defined for each Fourier component.

## 2.2 Velocity diffusion

The evolution of the electron velocity distribution function is described by the following Fokker-Planck equation,

$$\frac{\partial F}{\partial \hat{t}} = \frac{\partial}{\partial u} \hat{D}_w \frac{\partial F}{\partial u} + \frac{\partial}{\partial u} \left[ (\hat{D}_{ei} + \hat{D}_{ee}) \left( \frac{\partial F}{\partial u} + uF \right) \right], \quad (8)$$

where  $u \equiv v_z / v_e$  is the normalized parallel velocity and  $\hat{t} \equiv t \nu_0$  is the normalized time ( $v_e = (T_e / m)^{1/2}$ ; the electron thermal speed and  $\nu_0 = e^4 n_e \ln \Lambda / (2\pi \epsilon_0^2 m^{1/2} T_e^{3/2})$ ; the e-e collision frequency). In deriving Eq.(8), we assume a Maxwellian distribution with the temperature  $T_e$  in the perpendicular direction to the magnetic field and integrate the original linearized Fokker-Planck equation over that direction. The normalized quasi-linear diffusion coefficient,  $\hat{D}_w = D_w / \nu_0 v_e^2$ , is given by

$$\hat{D}_w(u, x) = \frac{e^2}{2m^2 \nu_0 v_e^2} \sum_n \frac{A_n(a_n a_n^*)}{(\omega - k_n v_z)^2 + A_n^2}, \quad (9)$$

$$(a_n^* a_n) = \left( |E_{zn}|^2 + \rho_e^2 E_{zn}^* \frac{\partial^2 E_{zn}}{\partial x^2} \right) - 2 \left( \frac{v_e}{v_{p,n}} \right)^2 \rho_e^2 E_{yn}^* \frac{\partial^2 E_{yn}}{\partial x^2}$$

$$+ \left( \frac{v_e}{v_{p,n}} \right) \rho_e \left( E_{zn} \frac{\partial E_{yn}}{\partial x} - E_{zn} \frac{\partial E_{zn}}{\partial x} \right), \quad (10)$$

where  $v_{p,n} = \omega/k_n$  is the phase velocity of the  $k_n$  mode. The width of the resonance,  $\Delta_n$ , is assumed to be given by the maximum value of the collision frequency or the trapping frequency due to the electric and magnetic field,

$$\Delta_n = \max \left[ v_e(v_{p,n}), \sqrt{\frac{ek_n |E_{zn}|}{m}}, k_n v_e \sqrt{\frac{\tilde{B}_{zn}}{2B(x)}} \right], \quad (11)$$

where  $\tilde{B}_{zn} = \omega^{-1} |\partial E_{yn}/\partial x|$ , and  $v_e (= (D_{ei} + D_{ee})/v_e^2)$  (see Eq.(12)) is the velocity dependent collision frequency. The  $v_e$ -dependence in the magnetic trapping is simply estimated by the electron thermal velocity  $v_e$ . Each term in Eq.(10) is the contribution from the electron Landau damping, the TTMP and the cross term between  $E_y$  and  $E_z$ , corresponding to each term in Eq.(5).

The normalized electron-ion(e-i) and electron-electron(e-e) collision coefficients,  $\hat{D}_{ei} = D_{ei}/\nu_0 v_e^2$  and  $\hat{D}_{ee} = D_{ee}/\nu_0 v_e^2$ , are given by

$$\hat{D}_{ei} = \frac{Z_{eff} G(u^2/2)}{4\sqrt{2}}, \quad (12-a)$$

$$\hat{D}_{ee} = \frac{1}{3\sqrt{2\pi} + |u|^3}, \quad (12-b)$$

where  $Z_{eff} = \sum_{s(\text{ion})} Z_s^2 n_s / n_e$  is the effective ion charge state and  $G(x) = \sqrt{\pi} \exp(x) [1 - \phi(\sqrt{x})(1-2x) - 2\sqrt{x}]$ . As for the e-e collision coefficient, Eq.(12-b), we interpolate between solutions in the high velocity region,  $u \gg 1$ , and those in the lower velocity region,  $1 \gg u$ .

The steady state solution of Eq.(8) is easily obtained as

$$F(u) = C \exp \left[ - \int_0^u \frac{u du}{1 + \hat{D}_w / (\hat{D}_{ei} + \hat{D}_{ee})} \right], \quad (13)$$

where the constant  $C$  is determined from the conservation of particle number. The DC current induced by the resonant electrons,  $J_r(x) = -en_e v_e \int_{-\infty}^{\infty} u F(u) du / \sqrt{2\pi}$ , is simply calculated from Eq.(13).

### 2.3 Current by bulk electrons

Some attentions have to be paid to estimate the induced current

according to the simplification in the velocity space treatment. In deriving the collision coefficient in Eq.(12), we have used the linearized version of the collision operator by replacing the integrand  $f_e(\vec{v})$  in the collision integral by the bulk distribution,  $f_e^b(\vec{v})$ , as  $C_{ee}(f_e, f_e) = C_{ee}(f_e, f_e^b)$ . In this approximation, the bulk electrons,  $f_e^b(\vec{v})$ , works as the sink of the momentum and energy transferred from the resonant electrons through e-e collision, although the nonresonant bulk electrons can sustain the current. This is the reason why the linearized Fokker-Planck solution underestimates the efficiency compared with the nonlinear treatment [15,16]. The additional induced current produced by nonresonant bulk electrons can be estimated as follows. The momentum balance equation for bulk electrons is expressed as

$$\frac{\partial}{\partial t} \int_{-\infty}^{\infty} f_e^b v_z dv_z = \int_{-\infty}^{\infty} C_{ei}(f_e^b, f_i) v_z dv_z + \int_{-\infty}^{\infty} C_{ee}(f_e^b, f_e) v_z dv_z, \quad (14)$$

where  $f_e$  is the electron distribution function in the z-direction modified by the wave field. Assuming the shifted Maxwellian with the drift velocity,  $v_d = v_e u_d$ , in the bulk distribution as  $f_e^b \propto \exp[-(u-u_d)^2/2]$ , the first term of the RHS in Eq.(14) is calculated from Eq.(12-a) as

$$\int_{-\infty}^{\infty} C_{ei}(f_e^b, f_i) v dv = n_e v_d \langle \nu_{ei} \rangle, \quad (15)$$

where  $\langle \nu_{ei} \rangle$  is the effective e-i collision frequency given by

$$\langle \nu_{ei} \rangle = -\frac{\nu_0}{\sqrt{2\pi}} \int_{-\infty}^{\infty} \hat{D}_{ei}(u) \exp[-(u-u_d)^2/2] du \approx \frac{Z_{eff} \nu_0}{3\sqrt{2}}.$$

By employing Eq.(15), we evaluate the additional current,  $J_b = -en_e v_d$ , from Eq.(14) in the steady state as

$$J_b = -\frac{e}{\langle \nu_{ei} \rangle} \int_{-\infty}^{\infty} C_{ee}(f_e, f_e^b) v dv = \frac{en_e v_e \nu_0}{\sqrt{2\pi} \langle \nu_{ei} \rangle} \int_{-\infty}^{\infty} \frac{u \hat{D}_{ee} \hat{D}_W}{(\hat{D}_{ee} + \hat{D}_{ei}) + \hat{D}_W} du, \quad (16)$$

where the momentum conservation relation,  $\int C_{ee}(f_e^b, f_e) v_z dv_z \approx -\int C_{ee}(f_e, f_e^b) v_z dv_z$ , is used.

## 2.4 Current-drive efficiency

In the following numerical calculation, the total induced current,  $J$ , is estimated by  $J=J_r+J_b$ . A normalized current-drive efficiency is then defined as

$$\hat{\eta}(x) = \frac{J}{P_{ef}} \frac{m\nu_0\nu_e}{e}, \quad (17)$$

where  $P_{ef}$  is the electron power absorption given by

$$P_{ef}(x) = \nu_e^3 \nu_0 m \int_{-\infty}^{\infty} \frac{u^2 F(u) du}{1 + \hat{D}_w / (\hat{D}_{ci} + \hat{D}_{ce})}. \quad (18)$$

Figure 1 illustrates the normalized efficiency as a function of the normalized phase velocity,  $u_p = \nu_p / \nu_e$  for the cases without additional current (dashed line) and with additional current (solid line). The effective electric field for the velocity diffusion is chosen as  $(a_n^* a_n)^{1/2} = 1 \text{ V/m}$  (see Eq.(10)). In the lower phase velocity region,  $u_p \lesssim 1$ , the efficiency is enhanced by 1.5 times by including the additional current. On the other hand, the correction in the high phase velocity region is small. This is due to the fact that the rate of the momentum transfer decreases with an increase of  $u_p$  according to Eq.(12-b). In the high phase velocity region, the result in Fig.1 reproduces the formula of the normalized efficiency given by

$$\hat{\eta} = \frac{2}{2 + \bar{Z}_{eff}} (u_2^2 - u_1^2) / \ln \frac{u_2}{u_1} \approx \frac{2}{2 + \bar{Z}_{eff}} u_1^2, \quad (19)$$

where the diffusion coefficient is non-zero in the region,  $u_2 \geq u \geq u_1$ , and the last formula assumes the condition,  $u_2 \gg u_2 - u_1$  [17].

In the limit of the zero resonance width ( $\Delta_0 \rightarrow 0$  in Eq.(9)) or the small input power, Eq.(18) reduces to the electron power absorption given by Eq.(5). In this case, the global current-drive efficiency,  $\eta_G$ , is defined as the ratio of the total induced current to the total emitted power from antennas (Eq.(7)) as

$$\eta_G = \int_{-\alpha}^{\alpha} J(x) dx / \bar{P}_A = \bar{J} / \bar{P}_A. \quad (20)$$

In addition to the effect of the bulk electrons, it is known that the effect of the pitch angle scattering, which induces the flattening of the distribution function in the  $v_{\perp}$ -direction, increases the current-drive efficiency. The dash-dotted line in Fig.1 shows the result of Cordey et al.[15] for the 2-dimensional treatment in the velocity space and the nonlinear collision operator. It is found that the efficiency obtained from the present 1-dimensional model(solid line) is two times lower in both regions of  $u_p \gg 1$  and  $u_p \ll 1$  and about 2.5 times lower around  $u_p = 2 \sim 3$ . Therefore, it may be appropriate to evaluate the current-drive efficiency to be 2~2.5 times larger than that obtained by the present 1-dimensional analysis.

### 3. Antenna design

In this section, we at first examine the accessibility condition of the wave in INTOR plasma. In subsection 3-2, we present the guideline of the antenna design for the efficient current-drive by using the phase shifted antenna array. The plasma parameters which simulate the INTOR are given in Table I. In the following calculation, we choose the wave frequency of 300MHz in the low field side(LFS) excitation from the requirement of the antenna design by using loop antennas. In the present parameters, harmonic number of  $l=6 \sim 8$  for deuterium and  $l=9 \sim 12$  for tritium is included inside the plasma column. Such higher harmonics absorption is examined to be small in the frequency range of  $f \gtrsim 250$  MHz from the calculation of the ray tracing code which is calculated in the same plasma parameters[18].

#### 3.1 Accessibility condition

The power absorption of the excited wave at a given antenna current is strongly dependent on the parallel wave number,  $k_n$ . The wave can be absorbed by electron only in the adequate region of  $k_n$ . Figure 2(a) illustrates the spectra of the power absorption by electrons,  $\bar{P}_e$ (solid line), and by the wall,  $\bar{P}_w$ (dashed line), as a function of the parallel wave number,  $n=k_n R_0$ , in the case of  $T_{e0}=30\text{keV}$  and the antenna current  $\hat{J}(k_n)=1\text{kA}$ . Figure.2(b) shows the same spectra versus the normalized phase velocity,  $u_{p0}=\omega/k_n v_{e0}$  ( $v_{e0}$  is the electron thermal velocity at the plasma center). These figures are considered as the accessibility condition which represents the coupling efficiency between wave and plasma.

In addition to the effect of the bulk electrons, it is known that the effect of the pitch angle scattering, which induces the flattening of the distribution function in the  $v_{\parallel}$ -direction, increases the current-drive efficiency. The dash-dotted line in Fig.1 shows the result of Cordey et al.[15] for the 2-dimensional treatment in the velocity space and the nonlinear collision operator. It is found that the efficiency obtained from the present 1-dimensional model(solid line) is two times lower in both regions of  $u_p \gg 1$  and  $u_p \ll 1$  and about 2.5 times lower around  $u_p = 2 \sim 3$ . Therefore, it may be appropriate to evaluate the current-drive efficiency to be 2~2.5 times larger than that obtained by the present 1-dimensional analysis.

### 3. Antenna design

In this section, we at first examine the accessibility condition of the wave in INTOR plasma. In subsection 3-2, we present the guideline of the antenna design for the efficient current-drive by using the phase shifted antenna array. The plasma parameters which simulate the INTOR are given in Table I. In the following calculation, we choose the wave frequency of 300MHz in the low field side(LFS) excitation from the requirement of the antenna design by using loop antennas. In the present parameters, harmonic number of  $l=6 \sim 8$  for deuterium and  $l=9 \sim 12$  for tritium is included inside the plasma column. Such higher harmonics absorption is examined to be small in the frequency range of  $f \gtrsim 250$  MHz from the calculation of the ray tracing code which is calculated in the same plasma parameters[18].

#### 3.1 Accessibility condition

The power absorption of the excited wave at a given antenna current is strongly dependent on the parallel wave number,  $k_{\parallel}$ . The wave can be absorbed by electron only in the adequate region of  $k_{\parallel}$ . Figure 2(a) illustrates the spectra of the power absorption by electrons,  $\bar{P}_e$ (solid line), and by the wall,  $\bar{P}_w$ (dashed line), as a function of the parallel wave number,  $n=k_{\parallel}R_0$ , in the case of  $T_{e0}=30\text{keV}$  and the antenna current  $\hat{J}(k_{\parallel})=1\text{kA}$ . Figure.2(b) shows the same spectra versus the normalized phase velocity,  $u_{p0}=\omega/k_{\parallel}v_{e0}$  ( $v_{e0}$  is the electron thermal velocity at the plasma center). These figures are considered as the accessibility condition which represents the coupling efficiency between wave and plasma.



From Fig.2, we give the lower limit of the toroidal wave number roughly as

$$k_{n,\min} \simeq \frac{\omega}{4v_{e0}}. \quad (21)$$

For  $k_n < k_{n,\min}$ , the launched wave is hardly absorbed by electrons because of the very small number of the resonant particles and the wall loss becomes dominant. Note here that  $k_{n,\min}$  depends not only on the frequency and temperature but also on the polarization of the parallel electric field,  $E_z/E_y$ . If the wave with the larger value of  $E_z/E_y$  is used,  $k_{n,\min}$  will take the smaller value than the present one.

The upper limit of the accessibility,  $k_{n,\max}$ , is determined by the cut-off of the fast wave which comes from the evanescent layer near the plasma boundary and estimated as follow. The distance between the plasma boundary ( $x=a$ ) and the fast wave cut-off ( $x=x_c$ ) is given from the cold dispersion relation as

$$|a-x_c| = \frac{\left\{ (n_{\parallel}^2 - 1) - \sum_s \frac{\omega_{psb}^2}{\Omega_s(\Omega_s + \omega)} \right\}}{\sum_s \frac{\omega_{ps0}^2}{\Omega_s(\Omega_s + \omega)} \left| \frac{1}{n_{s0}} \frac{\partial n_s}{\partial x} \right|_{x=a}}, \quad (22)$$

where  $\omega_{ps0}$  and  $\omega_{psb}$  are the plasma frequency of  $s$  species ion at the plasma center and the boundary,  $n_{\parallel} = k_{\parallel} c / \omega$ , and  $\Omega_s$  is the cyclotron frequency of  $s$  species ion evaluated at  $x=a$  assuming  $|a-x_c| \ll R_0$ . In the case of the parabolic density profile, Eq.(20) becomes

$$|a-x_c| \sim \frac{a}{2} (n_{\parallel}^2 - 1) \left/ \sum_s \frac{\omega_{ps0}^2}{\Omega_s(\Omega_s + \omega)} \right. . \quad (23)$$

Here, we neglect the edge density for simplicity. When the optical thickness,  $\int_{x_c}^a \text{Im}(k_x) dx \simeq \text{Im}(k_x) |a-x_c|$ , is larger than unity, the wave can not penetrate into the plasma. Then,  $k_{n,\max}$  is given from the condition,  $|a-x_c| \text{Im}(k_x) \simeq 1$  ;

$$k_{n,\max} \simeq \frac{\omega}{c} \left\{ 1 + \left[ \frac{4c}{a\omega} \sum_s \frac{\omega_{ps0}^2}{\Omega_s(\Omega_s + \omega)} \right]^{2/3} \right\}^{1/2}, \quad (24)$$

where  $\text{Im}(k_x) \approx (n_i^2 - 1)^{1/2} \omega / 2c$  is assumed. When the condition  $\omega \gg \Omega_s$  is satisfied, the relation,  $k_{n,\max} \propto (\omega n_{e0} / B_0)^{1/3}$ , is obtained from Eq.(24). In the present parameter listed in Table I,  $k_{n,\min} R_0 \approx 32$  and  $k_{n,\max} R_0 \approx 130$  are obtained from Eqs.(21) and (24) and these values are consistent with the result in Fig.2.

In Fig.2, we find sharp peaks especially in the high phase velocity region of  $u_p \gtrsim 2$ . These are due to the plasma cavity resonance[13,19]. The lower temperature case ( $T_{e0}=15\text{keV}$ ) is shown in Fig.3. The lower limit of the accessibility increase up to  $k_{n,\min} R_0 \approx 42$  although the upper limit is unchanged. It is found that the cavity resonance appears more remarkably in the lower temperature case. The cavity resonance was observed as was expected in the recent JT-60 experiment of the 2nd harmonic hydrogen heating[20]. The accessibility diagram such as Figs.2 and 3 is used to find the optimum antenna design for the efficient current-drive.

### 3.2 Phase shifted antenna array

In order to realize the efficient current-drive system, we apply an array of loop antennas. The total number of antenna is  $N$ , the antenna width in the  $z$ -direction is  $\Delta\omega$ , the  $z$ -spacing between two adjacent antennas is  $\Delta z$ , and the location of the center of  $j$ -th antenna is  $z_j = (j-1)\Delta z$  ( $j=1, 2, \dots, N$ ). The phase difference between two adjacent antenna is  $\Delta\phi$ , and the phase of the  $j$ -th antenna is  $\phi_j = (j-1)\Delta\phi$ . The spectrum of the antenna current is given by

$$|\hat{J}(k_n)| = 2J_0 \left| \frac{\sin(k_n \Delta\omega/2)}{k_n} \right| \left| \frac{1 - \cos N(\Delta\phi - k_n \Delta z)}{1 - \cos(\Delta\phi - k_n \Delta z)} \right|^{1/2}, \quad (25)$$

where  $J_0$  is the current density on each antenna element. The dominant spectrum peak and its width are estimated from Eq.(25) to be

$$k_m = \frac{\Delta\phi - 2\pi m}{\Delta z} \quad \text{for } m=0, \pm 1, \pm 2, \dots, \quad (26-a)$$

$$\Delta k = \frac{4\pi}{N\Delta z}. \quad (26-b)$$

We set up that the current is driven mainly by the  $m=0$  spectrum peak. At that time, the  $m=1$  spectrum peak induces the counter current and reduces

the current-drive efficiency unless the  $m=1$  spectrum peak is removed from the accessibility region, i.e.  $k_{m=1} < -k_{n,\max}$ . Therefore, we get the following condition for the antenna spacing ;

$$\Delta z \lesssim \frac{2\pi}{k_{n,\max} + k_{m=0}} \quad (27)$$

where  $k_{m=0}$  is the value of the  $m=0$  main spectrum peak by which the efficient current-drive is expected. To remove the  $m=1$  spectrum from the accessibility for the arbitrary change of  $\Delta\phi$  among  $0 \leq \Delta\phi \leq \pi$ ,  $\Delta z$  have to satisfy the relation,  $\Delta z \lesssim \pi/k_{n,\max}$ .

The optimum phase difference between two adjacent antennas is estimated for a fixed  $\Delta z$  as

$$\Delta\phi = \frac{\omega \Delta z}{v_e \alpha} \quad (28)$$

where  $\alpha = v_{p,m=0}/v_{e0}$  is the normalized phase velocity of the  $m=0$  spectrum peak and  $v_{p,m=0} = \omega/k_{m=0}$ . In the present plasma parameter listed in Table I,  $\alpha = 3 \sim 4$  is estimated for the efficient current-drive from Fig.2, i.e.  $\omega \Delta z / 3v_{e0} \gtrsim \Delta\phi \gtrsim \omega \Delta z / 4v_{e0}$ . The dependence of the current-drive efficiency on the phase difference is presented in detail in the next section.

The total antenna number,  $N$ , is determined from Eq.(26-b) to take  $\Delta k$  small so that the phase velocity of the excited wave is selected in the extent of the electron thermal velocity around the optimum phase speed. Since this condition is roughly estimated by  $\Delta k \simeq \omega/6v_e$ , assuming  $v_{p,m=0}/v_{e0} \simeq 3$  the total antenna number is given by

$$N \simeq \frac{24\pi v_{e0}}{\omega \Delta z} \quad (29)$$

In the present calculation, we take  $k_{m=0}R_0 \simeq 60$ , which corresponds to  $v_{p,m=0}/v_{e0} \simeq 3$  in Eq.(27). Then  $\Delta z \lesssim 0.17\text{m}$  is obtained. We select the total antenna number  $N=17$  which is estimated from Eq.(29) at  $T_{e0}=30\text{keV}$ . The antenna parameters are also shown in Table I. The spectrum of the antenna current is illustrated in Fig.4 for  $\Delta\phi=\pi$  case and other parameters in Table I. The power absorption is determined by the product between the absorption spectrum in Fig.2 and the antenna spectrum. Between dominant two peaks

of  $k_m$ ,  $N-2$  small subpeaks with small amplitude are found. The ratio of the amplitude between these subpeaks and  $k_m$  is roughly estimated from Eq.(25) as  $1/N$  and depends on the total antenna number. The subpeaks sometimes can not neglect and reduces the current-drive efficiency especially in the case of small  $N$ , because these spectra easily couple with the thermal component.

#### 4. Numerical results and analysis

In this section, we present numerical results on the fast wave current-drive under the launching condition which is chosen in the previous section. We show the phase dependence of the power absorption and the induced current in subsection 4-1. In subsection 4-2, we study the plasma parameter dependence of the global current-drive efficiency. We discuss about the performance of the fast wave current-driven tokamak reactor in subsection 4-3. In the following numerical calculation, we fix the total input power,  $\bar{P}_A=1\text{MW/m}$ . We have checked the effect of the input power on the power absorption and the induced current, and found that these values are almost unchanged by an increase of  $\bar{P}_A$  up to 80MW for the present plasma parameter. Therefore, we discuss the numerical results along the global current-drive efficiency defined by Eq.(20). In the following subsections, we introduce the angular unit,  $\Delta\tilde{\phi}=180^\circ\Delta\phi/\pi$ ,

##### 4.1 Phase dependence

Figure 5(a) shows the phase dependence of the average loading resistance and reactance per an antenna, i.e.  $\bar{R}=\sum_{j=1}^N \text{Re}(Z_j)/N$  and  $\bar{X}=\sum_{j=1}^N \text{Im}(Z_j)/N$ , where  $Z_j$  is the loading impedance of the  $j$ -th antenna defined by

$$Z_j = \int_{z_j-\Delta w/2}^{z_j+\Delta w/2} E_y(z) J_j^A(z) \exp(i\phi_j) dz / \left( \int_{z_j-\Delta w/2}^{z_j+\Delta w/2} J_j^A(z) dz \right)^2.$$

Figure 5(b) shows the phase dependence of the absorption by electrons,  $\bar{P}_e$ , and the wall loss,  $\bar{P}_w$ . The loading resistance is the lower value up to  $\Delta\tilde{\phi} \lesssim 60^\circ$  although the level of the electron absorption is 60~70% on average. The loading reactance is almost constant value for the change of  $\Delta\phi$ . The wave number,  $k_{m=0}$ , for  $\Delta\tilde{\phi} \lesssim 60^\circ$  ( $k_n R_0 \lesssim 30$ ) corresponds to the phase velocity of  $u_{p0} \gtrsim 4$  and this wave is hard to couple with bulk electrons(see Fig.2).

of  $k_m$ ,  $N-2$  small subpeaks with small amplitude are found. The ratio of the amplitude between these subpeaks and  $k_m$  is roughly estimated from Eq.(25) as  $1/N$  and depends on the total antenna number. The subpeaks sometimes can not neglect and reduces the current-drive efficiency especially in the case of small  $N$ , because these spectra easily couple with the thermal component.

#### 4. Numerical results and analysis

In this section, we present numerical results on the fast wave current-drive under the launching condition which is chosen in the previous section. We show the phase dependence of the power absorption and the induced current in subsection 4-1. In subsection 4-2, we study the plasma parameter dependence of the global current-drive efficiency. We discuss about the performance of the fast wave current-driven tokamak reactor in subsection 4-3. In the following numerical calculation, we fix the total input power,  $\bar{P}_A=1\text{MW/m}$ . We have checked the effect of the input power on the power absorption and the induced current, and found that these values are almost unchanged by an increase of  $\bar{P}_A$  up to 80MW for the present plasma parameter. Therefore, we discuss the numerical results along the global current-drive efficiency defined by Eq.(20). In the following subsections, we introduce the angular unit,  $\Delta\tilde{\phi}=180^\circ\Delta\phi/\pi$ ,

##### 4.1 Phase dependence

Figure 5(a) shows the phase dependence of the average loading resistance and reactance per an antenna, i.e.  $\bar{R}=\sum_{j=1}^N \text{Re}(Z_j)/N$  and  $\bar{X}=\sum_{j=1}^N \text{Im}(Z_j)/N$ , where  $Z_j$  is the loading impedance of the  $j$ -th antenna defined by

$$Z_j = \int_{z_j-\Delta w/2}^{z_j+\Delta w/2} E_y(z) J_j^A(z) \exp(i\phi_j) dz / \left( \int_{z_j-\Delta w/2}^{z_j+\Delta w/2} J_j^A(z) dz \right)^2.$$

Figure 5(b) shows the phase dependence of the absorption by electrons,  $\bar{P}_e$ , and the wall loss,  $\bar{P}_w$ . The loading resistance is the lower value up to  $\Delta\tilde{\phi} \lesssim 60^\circ$  although the level of the electron absorption is 60~70% on average. The loading reactance is almost constant value for the change of  $\Delta\phi$ . The wave number,  $k_{m=0}$ , for  $\Delta\tilde{\phi} \lesssim 60^\circ$  ( $k_n R_0 \lesssim 30$ ) corresponds to the phase velocity of  $u_{p0} \gtrsim 4$  and this wave is hard to couple with bulk electrons(see Fig.2).

In this region, the electron power absorption is caused by the subpeaks of the antenna spectrum not by the  $m=0$  spectrum peak as discussed in the previous subsection 3-2. As  $\Delta\tilde{\phi}$  increases, the antenna loading resistance increases and becomes maximum value around  $\Delta\tilde{\phi}=100^\circ$  ( $k_n R_0=50$ ). Figure 5(c) represents the phase dependence of  $\eta_e=\bar{J}/\bar{P}_e$  and the global current-drive efficiency  $\eta_G=\bar{J}/\bar{P}_A$ . The optimum phase is found around  $\Delta\tilde{\phi}\approx 80^\circ$  and then the efficiency gradually decreases with an increase of  $\Delta\tilde{\phi}$ . At  $\Delta\tilde{\phi}=80^\circ$ ,  $\eta_G\approx 0.075\text{A/W}$  is obtained. Figures 5(a) and (b) show that the optimum phase selection for the current-drive does not correspond to the optimum phase from the standpoint of the antenna loading. Namely, in order to improve the current-drive efficiency, the high phase velocity has to be chosen where the coupling efficiency between electron and wave is weak.

Figure 6(a), (b) and (c) show the spatial profiles of the electron power absorption,  $P_e(x)$ , the induced current,  $J(x)$ , and the normalized current-drive efficiency,  $\hat{\eta}(x)$ , in the case of  $\Delta\tilde{\phi}=80^\circ$ . The antenna spectrum is illustrated in Fig.6(d). Figures.6(e) and (f) illustrate the deviation of the parallel electron distribution function from the Maxwellian,  $F_e-F_M$ , and the normalized diffusion coefficient,  $\hat{D}_w(u)$ , at the center ( $x=0$ ). It is found in Figs.6(d)-(f) that waves around  $k_n R_0=40\sim 50$  ( $u_{p0}=3\sim 4$ ) are selectively excited according to the  $k_{m=0}$  spectrum peak. The almost center-peaked electron absorption and the induced current are obtained around the optimum antenna phase. Taking into account the underestimation of the efficiency which comes from the 1-D treatment in the velocity space as was pointed out in section 2-3, we can expect the global efficiency of  $\eta_G\approx(0.15\sim 0.18)\text{A/W}$  around  $\Delta\tilde{\phi}=80^\circ$ . Here, we multiply  $\eta_G$  by the factor  $2\sim 2.4$  which is estimated from Fig.1 and Figs.6(e). The corrugation of the power absorption and the induced current are due to the standing wave formation. In order to see this feature, the wave pattern of  $|E_y(x)|$  and  $|E_z(x)|$  are shown in Figs.7(a) and (b) for  $k_n R_0=40$ , which corresponds to the  $m=0$  spectrum peak for  $\Delta\tilde{\phi}=80^\circ$ . Since the coupling efficiency between the wave and electrons is weak due to the high phase velocity, the incident wave launched from LFS antenna is not completely absorbed in a single pass and reflected back at the HFS wall. In the result, the standing wave is formed. In this case, electrons absorb the power in a multi-pass process.

Figures 8 and 9 show the same spatial profile as Figs.6(a)-(c) in the case of  $\Delta\tilde{\phi}=100^\circ$  (Fig.8) and  $\Delta\tilde{\phi}=140^\circ$  (Fig.9). The strong corrugation which is seen in the  $\Delta\tilde{\phi}=80^\circ$  case disappears in the case of  $\Delta\tilde{\phi}=100^\circ$ . Since the phase

velocity of the  $k_{m=0}$  spectrum peak is small compared with the  $\Delta\phi=80^\circ$  case, electrons absorb the wave power almost in a single pass until wave reaches the HFS wall. In the case of  $\Delta\phi=140^\circ$ , it is found that the maximum point of the power absorption and the induced current profile shift to the LFS ( $x\sim 0.4\text{m}$ ). Figures 10(a) and (b) also show the same wave pattern as Fig.7 for  $k_n R_0=70$  corresponding to the  $k_{m=0}$  spectrum peak for  $\Delta\phi=140^\circ$ . It is found that the standing wave ratio is small both in  $E_y$  and  $E_z$  components showing the travelling wave in the region,  $-0.5\text{m}\lesssim x\lesssim 1.15\text{m}$ . Furthermore, it is found that the amplitude of the  $E_z$  component decreases near the center. This is because the strong absorption by electrons occurs before the launched wave reaches the center.

The deviation of the maximum point of the absorbed power and the induced current profiles from the center is shown in Fig.11. With an increase of the antenna phase from  $\Delta\phi\approx 100^\circ$ , the maximum point of the induced current shifts to the LFS accompanied with the decrease of the induced current. This result shows the possibility of the current profile control in the high temperature and high density plasma regime by changing the antenna phase difference.

The dependence of the efficiency on the total antenna number,  $N$ , is shown in Fig.12 in the case of  $\Delta\phi=80^\circ$  and  $\Delta\phi=120^\circ$ . In the case of  $\Delta\phi=80^\circ$ , the efficiency decreases with decreasing the total antenna number. This is considered as follows. With a decrease of  $N$ , the width of the  $m=0$  spectrum peak,  $\Delta k$ , spreads according to Eq.(26-b). Due to the spread of  $\Delta k$ , waves with the higher toroidal wave number becomes accessible. Since the wave with the higher toroidal wave number has a good coupling efficiency, the input power is absorbed by these waves and resultantly the driving efficiency decreases. The relatively weak dependence of  $\eta_G$  on  $N$  is due to the cavity resonance. That is, the strong cavity wave is observed around  $k_n R_0=40$  as seen in Fig.2. This cavity wave still induces the significant part of the induced current even if the width of the spectrum peak spreads. This result shows that the dependence of the driving efficiency on the total antenna number is weak when the wave propagation is dominated by the plasma cavity resonance. In the case of  $\Delta\phi=120^\circ$  ( $k_n R_0=60$ ),  $\eta_G$  remains almost the constant value up to about  $N=7$ . In this case, not only the waves with the higher toroidal wave number but also the waves with the lower one also becomes accessible as seen in Fig.2(a). The waves with the higher toroidal wave number also decreases the efficiency as in the case of  $\Delta\phi=80^\circ$ . However, since the waves with

the lower toroidal wave number can efficiently drive the current, the global efficiency is kept to the almost constant value.

Here, we have employed the slab geometry. In the 1-dimensional wave propagation model, the cavity resonance tends to be easily excited especially in the case that the wave absorption is weak. However, the 2-dimensional analysis of the fluid plasma shows that the strength of the cavity resonance is suppressed compared with the slab geometry because of the freedom in the poloidal direction [22]. Therefore, the dependence of the efficiency on the total antenna number may be more remarkable when the cavity resonance is suppressed.

#### 4.2 Plasma parameter dependence

The minimum wave number,  $k_{n,\min}$ , depends on the temperature as seen in Eq.(21). Therefore, the antenna phase has to be changed according to Eq.(28) in order to maximize the induced current for the change of the temperature. Figure 13 shows the temperature dependence of the efficiency in the case of  $n_{e0}=10^{20}\text{m}^{-3}$ . Assuming that  $\Delta\phi_{\text{opt}}$  is the optimum phase for the temperature  $T_0$ , Eq.(28) becomes  $\Delta\phi = \Delta\phi_{\text{opt}}\sqrt{T_0/T_e}$ . In Fig.11, the antenna phase is changed according to the above relation. It is found that the linear dependence of the efficiency on the temperature is roughly obtained. This result is predicted from Eq.(14), i.e.  $J/P_{\text{eff}} \simeq \eta(x \simeq 0)e/mv v_e \propto T_{e0}$ .

The density dependence of the efficiency is shown in Fig.14 in the case of  $T_{e0}=30\text{keV}$ . An inverse dependence of  $\eta_G$  on the density is observed. Note here that with an increase of the density, the maximum wave number,  $k_{n,\max}$ , increase according to Eq.(24). Therefore, we have to pay an attention to the  $m=1$  antenna spectrum peak,  $k_{m=1}$ , for the fixed antenna spacing  $\Delta z$ . In the present antenna spacing ( $\Delta z=0.17\text{m}$ ), the  $m=1$  spectrum peak does no affect on the efficiency up to  $\Delta\tilde{\phi} \simeq 100^\circ$  even in the high density case such as  $n_{e0}=1.5 \times 10^{20}\text{m}^{-3}$ .

Figure 15 show the  $Z_{\text{eff}}$  dependence of  $\eta_G$  in the case of  $T_{e0}=30\text{keV}$  and  $n_{e0}=10^{20}\text{m}^{-3}$ . In the calculation, we only change the value of  $Z_{\text{eff}}$  in Eq.(12-a) assuming that a small number of impurity ions does not considerably change the wave propagation. The dependence of  $\eta_G \propto (Z_{\text{eff}}+2)^{-1}$  given by Eq.(19) is obtained in Fig.15.

From Figs.13-15, we can roughly estimate the RF power,  $P_{\text{RF}}$ , needed to sustain the steady state current,  $I_p$ , around the optimum antenna phase,  $\Delta\tilde{\phi} \simeq 80^\circ \sqrt{30/T_{e0}}$ , as



$$P_{RF} = \frac{C_{RF} R_0 I_p n_{e0} (Z_{eff} + 2)}{T_{e0}} \quad (30)$$

where  $P_{RF}$  is in unit of MW,  $I_p$  in MA,  $T_{e0}$  in keV and the numerical constant  $C_{RF}$  is given by  $C_{RF} \approx (0.9 \sim 1.1) \times 10^{-19}$  in the present parameter. Here we multiply  $n_G$  by the factor 2.0~2.4 as the two-dimensional effect in the velocity space which is estimated from Fig.1 and Figs.6(e) and (f). In the next subsection, we study the performance of the present fast wave current-drive as a tokamak reactor by using Eq.(30).

#### 4.3 Performance of tokamak reactor

Now, we discuss about the performance of a reactor with the major radius  $R_0$ , the minor radius  $a$  and the ellipticity  $\kappa$ . The plasma current,  $I_p$ , is sustained by the applied fast wave, and the input power,  $P_{RF}$ , is assumed to be given only by this RF wave. Characteristics of a lower hybrid wave driven tokamak reactor was studied by Yuen et al. [17].

By using Eq.(30) for the current-drive efficiency, we can easily estimate the fusion energy multiplication factor,  $Q = P_f / P_{RF}$ . When both profiles of the density and the temperature are assumed to be parabolic in the radial direction, the fusion output power,  $P_f$ , is given as

$$\begin{aligned} P_f &= W_f \int n_D n_T \langle \sigma v \rangle_{DT} dv \\ &= 2.53 \times 2\pi^2 \kappa a^2 R_0 \frac{n_{D0} n_{T0}}{10^{40}} \left( \frac{T_{i0}}{20} \right)^{1.73} U(T_{i0}), \end{aligned} \quad (31)$$

where the released energy per one DT fusion reaction,  $W_f$ , is considered to be 17.6 MeV, subscript 0 denotes the central value,  $W_f$  is in unit of MW, and  $T$  in keV. The reactivity for a DT Maxwellian plasma,  $\langle \sigma v \rangle_{DT}$ , is given as a function of the ion temperature,  $T_i = T_D = T_T$  [21], and the correction factor,  $U(T_{i0})$ , for the case of parabolic profiles is approximated by

$$U(T_{i0}) \approx 1 - 0.3 \left\{ \frac{\ln(T_{i0}/20)}{\ln 2} \right\}^2$$

in the range,  $10 \text{ keV} < T_{i0} < 40 \text{ keV}$ .

From Eqs.(30) and (31), we obtain the  $Q$  value ;

$$Q = \frac{1.25 \times 10^{-19}}{C_{RF}} \frac{\kappa \alpha^2}{I_p (2 + Z_{eff})} \frac{4 n_{D0} n_{T0}}{n_{e0}^2} \frac{n_{e0}}{10^{20}} T_{e0} \left( \frac{T_{i0}}{20} \right)^{1.73} U(T_{i0}) \quad (32-a)$$

$$= \frac{4.66 \times 10^{-18}}{C_{RF}} \frac{\kappa \alpha^2}{I_p (2 + Z_{eff})} \frac{4 n_{D0} n_{T0}}{n_{e0}^2} \frac{2 T_{e0}}{T_{e0} + T_{i0}} B_0^2 \beta \left( \frac{T_{i0}}{20} \right)^{1.73} U(T_{i0}) \quad (32-b)$$

where the beta value is defined as  $\beta = 2\mu_0 \bar{p} / B_0^2$ ,  $\bar{p} = 1.6 \times 10^{-18} n_{e0} (T_{e0} + T_{i0}) / 3$  is the volume averaged plasma pressure,  $I_p$  is in unit of MA,  $B_0$  in Tesla. By introducing the critical beta value,  $\beta_c$ , based on the MHD stability condition,

$$\beta_c = 10^{-2} g_T \frac{I_p}{\alpha B_0},$$

where  $g_T$  denotes the "Troyon coefficient" of the order of unity, we rewrite Eq.(32-b) by using the value of  $C_{RF}$  obtained in the previous subsection,  $C_{RF} \approx 1.0 \times 10^{-19}$ , as

$$Q = 0.37 (g_T \kappa \alpha B_0) \frac{4 n_{D0} n_{T0}}{n_{e0}^2 (Z_{eff} + 2)} \frac{2 T_{e0}}{T_{e0} + T_{i0}} \frac{\beta}{\beta_c} \left( \frac{T_{i0}}{20} \right)^{1.73} U(T_{i0}).$$

Therefore, the  $Q$  value can be enlarged by the increase of the value of  $(g_T \kappa \alpha B_0)$  and by the increase of the temperature under the condition of the constant pressure. For the parameters listed in Table I,  $I_p$  must be greater than 5.6MA to satisfy the condition  $\beta < \beta_c$  assuming  $g_T = 3$ ,  $P_{RF}$  is about 34MW for  $I_p = 5.6$ MA,  $P_f$  is about  $(146\kappa)$ MW, and then  $Q$  value becomes about  $4.3\kappa$ .

## 5. Concluding remarks

We have studied analytically and numerically the fast wave current-drive in the high density and high temperature plasma regime which simulates the INTOR plasma. In order to get the optimum launching condition, we have investigated the accessibility of the fast wave and then determined the antenna condition such as the spacing between two adjacent antennas and the total antenna number. The antenna spacing is determined so that the  $m=1$  spectrum peak is removed from the accessibility condition to avoid the counter current generation. The total antenna number is determined so that the spread of the phase velocity of the excited wave is a level of the electron thermal velocity.

After determining the antenna condition, we have examined the phase dependence of the antenna loading impedance, the power absorption and the current-drive efficiency. For a fixed antenna condition, the optimum antenna phase is found and the global efficiency,  $\eta_G \approx 0.075 A/W$ , is obtained in the case of  $n_{e0} = 10^{20} m^{-3}$  and  $T_{e0} = 30 keV$  within the framework of the 1-dimensional velocity space treatment in the Fokker-Planck equation. This value corresponds to about  $(0.15 \sim 0.18) A/W$  if we take into account the 2-dimensional effect in the velocity space and reaches the value of  $(0.48 \sim 0.58)$  in the efficiency definition given by  $\bar{n}_e (10^{20} m^{-3}) I_p(A) R(m) / P_{RF}(W)$ .

Around the optimum antenna phase, the center-peaked current-profile with small corrugation is obtained. The corrugation in the current profile is due to the standing wave formation of the excited wave which comes from the weak coupling between wave and plasma. In this case, the wave absorption takes place in the multi-pass process. We also find that the antenna loading resistance is small around the optimum antenna phase. This result indicates that the larger antenna current is needed to sustain the constant plasma current. With an increase of the antenna phase difference from the optimum one, the total loading resistance increases and the corrugation in the induced current profile disappears. It is also found that the maximum point of the induced current shifts to the plasma surface. This result shows the possibility of the current profile control by the change of the antenna phase.

We have also studied the performance of the fast wave current-driven tokamak reactor by examining the fusion energy multiplication factor,  $Q$ . From the numerical calculation for the temperature and density dependences

on the driving efficiency, we find the relation,  $P_{RF} = C_{RF} R_0 I_p n_{e0} (Z_{eff} + 2) / T_{e0}$ , which is expected from Eq.(17), and the numerical constant,  $C_{RF}$ , is determined. The above relation is used to estimate the  $Q$ -value. We find that the  $Q$  value is almost proportional to  $\kappa \alpha B_0 T_{e0}^{1.73} (\beta / \beta_c)$  and shows the strong dependence on the temperature under the condition of the constant plasma pressure. This result means that the higher temperature and the lower density plasma is more efficient for a tokamak reactor when the plasma current is sustained by the RF wave. In the present calculation,  $Q \approx 4.3\kappa$  is obtained for  $T_{e0} = 30 \text{ keV}$  and  $n_{e0} = 10^{20} \text{ m}^{-3}$ .

In order to improve the current-drive efficiency, excitation of the wave with the higher phase velocity is expected. In the present calculation, the maximum phase velocity which can contribute to the current-drive is limited by the wall loss as seen in Figs.2 and 3. The ratio,  $P_e(k_n) / P_w(k_n)$  depends on the distance between the plasma surface,  $x=a$ , and the antenna location,  $x=d$ , for the fixed wall radius (see Eq.(6)). Therefore, the locations of antenna and the plasma surface are important parameters. Another method is to increase the exciting frequency. That is, the polarization of the parallel electric field,  $E_z / E_y$ , depends on the frequency and becomes larger value with an increase of the frequency. However, the cut-off density becomes higher and the accessibility region for the electron power absorption, i.e.  $k_{n,\max} < |k_n| < k_{n,\min}$ , becomes narrower because of the dependence of  $k_{n,\min} \propto \omega$  and  $k_{n,\max} \propto \omega^{1/3}$  (see Eqs.(21) and (25)). The optimization including the frequency dependence is also needed in the further analysis.

#### Acknowledgements

The authors would like to thank Drs. T.Yamamoto, N.Fujisawa, K.Ushigusa, M.Yamagiwa and T.Tuda for their valuable discussions and comments. We wish to express sincere thanks to Dr. K.Odajima and ICRF group of JAERI for their useful discussions. Thanks are due to Dr. M.Tanaka and Dr. T.Takeda for their continuous encouragement.

on the driving efficiency, we find the relation,  $P_{RF} = C_{RF} R_0 I_p n_{e0} (Z_{eff} + 2) / T_{e0}$ , which is expected from Eq.(17), and the numerical constant,  $C_{RF}$ , is determined. The above relation is used to estimate the  $Q$ -value. We find that the  $Q$  value is almost proportional to  $\kappa a B_0 T_{e0}^{1.73} (\beta / \beta_c)$  and shows the strong dependence on the temperature under the condition of the constant plasma pressure. This result means that the higher temperature and the lower density plasma is more efficient for a tokamak reactor when the plasma current is sustained by the RF wave. In the present calculation,  $Q \simeq 4.3\kappa$  is obtained for  $T_{e0} = 30 \text{ keV}$  and  $n_{e0} = 10^{20} \text{ m}^{-3}$ .

In order to improve the current-drive efficiency, excitation of the wave with the higher phase velocity is expected. In the present calculation, the maximum phase velocity which can contribute to the current-drive is limited by the wall loss as seen in Figs.2 and 3. The ratio,  $P_e(k_n) / P_w(k_n)$  depends on the distance between the plasma surface,  $x=a$ , and the antenna location,  $x=d$ , for the fixed wall radius (see Eq.(6)). Therefore, the locations of antenna and the plasma surface are important parameters. Another method is to increase the exciting frequency. That is, the polarization of the parallel electric field,  $E_z / E_y$ , depends on the frequency and becomes larger value with an increase of the frequency. However, the cut-off density becomes higher and the accessibility region for the electron power absorption, i.e.  $k_{n,max} < |k_n| < k_{n,min}$ , becomes narrower because of the dependence of  $k_{n,min} \propto \omega$  and  $k_{n,max} \propto \omega^{1/3}$  (see Eqs.(21) and (25)). The optimization including the frequency dependence is also needed in the further analysis.

### Acknowledgements

The authors would like to thank Drs. T.Yamamoto, N.Fujisawa, K.Ushigusa, M.Yamagiwa and T.Tuda for their valuable discussions and comments. We wish to express sincere thanks to Dr. K.Odajima and ICRF group of JAERI for their useful discussions. Thanks are due to Dr. M.Tanaka and Dr. T.Takeda for their continuous encouragement.

## Reference

- 1) YAMAMOTO,T., IMAI,T., SHIMADA,M., SUZUKI,N., MAENO,M., et al.,  
Phys. Rev. Lett.45(1980)716.
- 2) MAEKAWA,T., SAITO,T., NAKAMURA,M., CHO,T., KUBO,W., et al.,  
Phys. Lett. 85A(1981)339.
- 3) LUCKHARDT,S.C., PORKLAB,M., KNOWLTON,S.F., CHEN,K.-I.,  
FISHER,A.S., et al., Phys. Rev. Lett. 48(1982)152.
- 4) BERNABEI,S., DAUGHNEY,C., EFTHIMION,P., HOOKE,W., HOSEA,J., et  
al.,Phys. Rev. Lett. 49(1982)1255.
- 5) JT-60 Team presented by T.Imai, in 11th Int. Conf. on Plasma Physics  
and Controlled Nuclear Fusion Research, Kyoto, 1986, IAEA-CN-47.
- 6) YAMAMOTO,T., and JFT-2M GROUP, in Noninductive Current-Drive in  
Tokamaks (Proc. IAEA Tech. Committee Meeting, Culham,1983),  
Vol.1(1983)224.
- 7) Hook,W., Plasma Phys. Contr. Fusion, 26, (1984)133.
- 8) UESUGI,Y., YAMAMOTO,T., HOSHINO,K., OHTSUKA,H.,  
KAWASHIMA,H., et al., in Controlled Fusion and Plasma  
Physics( Proc. 14th Europ. Conf. Madrid, 1987), Vol. 11D, Part  
3(1987)942.
- 9) YAMAMOTO,T., UESUGI,Y., HOSHINO,K., KAWASHIMA,H.,  
OHTSUKA,H., Numerical Study of the Electron Heating and Current  
Drive by the Fast Waves in the JFT-2M Tokamak Plasma, JAERI-M  
86-115(1986).
- 10) ANDO,R., KAKO,E., OGAWA,Y., WATARI,T., Nucl. Fusion  
26(1986)1619.
- 11) EAST,D.A., EVANS,K.,Jr, IGNAT,D.W., Nucl. Fusion 26(1986)461.
- 12) ANDREWS,P.L., BHADRA,D.K., Nucl. Fusion 26(1986)897.
- 13) KISHIMOTO,Y., HAMAMATSU,K., FUKUYAMA,A., ITOH,S.-I., ITOH,K.,  
Nucl. Fusion 27(1987)549.
- 14) FUKUYAMA,A., NISHIYAMA,S., ITOH,K., ITOH,S.I., Nucl. Fusion  
23(1983)1005.
- 15) CORDEY,J.G., EDLINGTON,T., START,D.F.H., Plasma Phys. 24(1982)73.
- 16) HARVEY,R.W., Marx,K.D., MaCoy,M.G., Nucl. Fusion 21(1981)153.
- 17) YUEN,S.Y., KAPLAN,D., COHN,D.R., Nucl. Fusion 20(1980)159.
- 18) USHIGUSA,K., private communication.
- 19) HAMAMATSU,K., KISHIMOTO,Y., FUKUYAMA,A., ITOH,K., ITOH,S.I.,  
AZUMI,M., Jpn. J. Appl. Phys., 26,No.9(1987).

- 20) SAIGUSA, M., KOBAYASHI, N., KIMURA, H., FUJII, T., HAMAMATSU, K.,  
in Proceedings of 7-th Topical Conf. on Application of Radio-Frequency  
Power to Plasmas, Kissimme, 1987.
- 21) TAKIZUKA, T., YAMAGIWA, M., Reactivity for DT Plasma with  
Beam-Induced Tail in the Magnetic Confinement System, JAERI-M  
87-066(1987).
- 22) ITOH, K., ITOH, S.I., FUKUYAMA, A., Nucl. Fusion 24(1984)13.

Table 1 Standard plasma- and antenna-parameters simulating the INTOR plasma

major radius	$R_0$	4.9 m
minor radius	$a$	1.15 m
antenna radius	$d$	1.25 m
wall radius	$b$	1.30 m
toroidal field	$B_0$	5.5 T
wall conductivity	$\sigma_w$	$10^{-5}(\Omega m)^{-1}$
temperature	$T_{e0} = T_{D0} = T_{T0}$ ( $\bar{T}_e$ )	30 keV (20 keV)
density	$n_{e0} = 2n_{D0} = 2n_{T0}$ ( $\bar{n}_e$ )	$1 \times 10^{20} m^{-3}$ ( $0.67 \times 10^{20} m^{-3}$ )
edge temperature	$T_b/T_0$	0.01
edge density	$n_b/n_0$	0.05
frequency	$f (= \omega/2\pi)$	300 MHz
antenna width	$\Delta w$	0.1 m
antenna spacing	$\Delta z$ ( $\Delta\theta = 180^\circ \Delta z / \pi R$ )	0.17 m ( $2^\circ$ )
antenna number	$N$	17



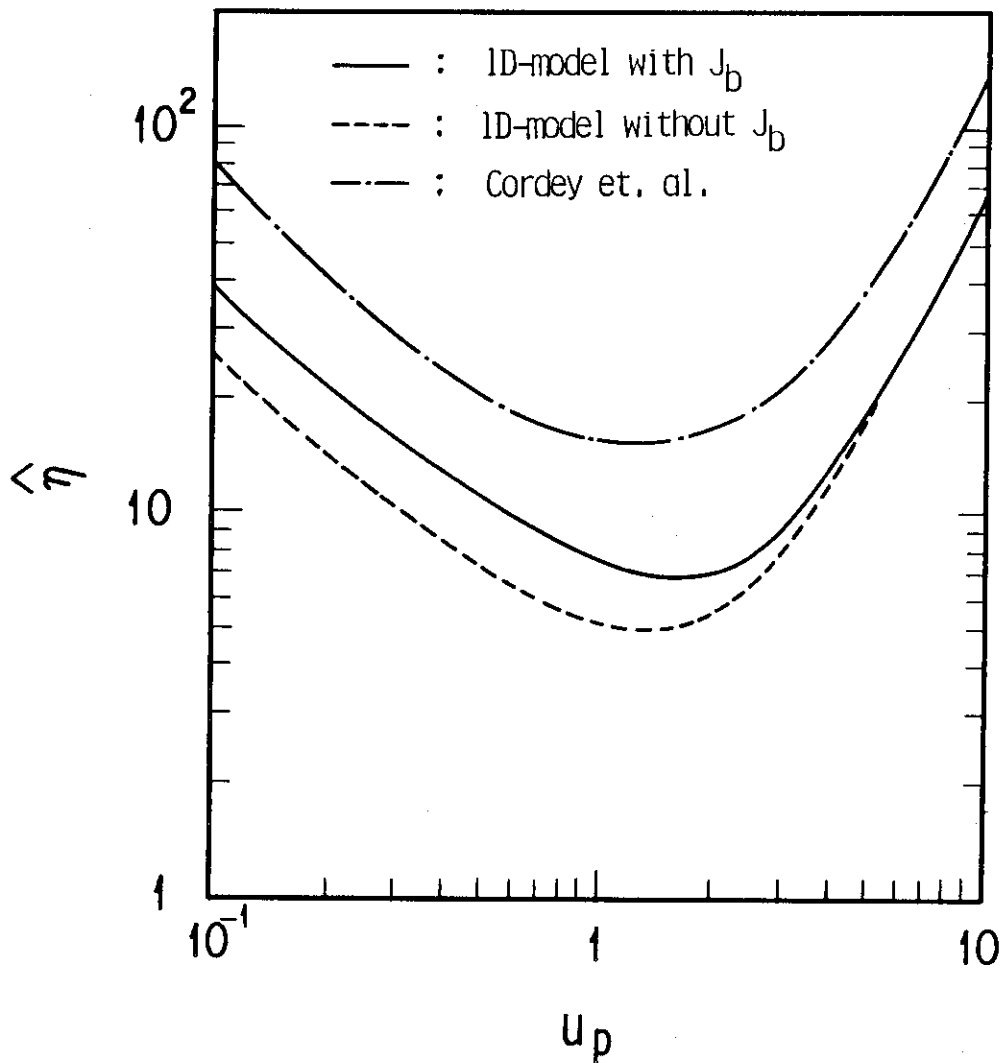


Fig.1 Normalized efficiency factor,  $\hat{\eta}$ , versus  $u_p (\equiv v_p/v_e)$  for three different models. Results of the 1-dimensional model with the additional current by bulk electrons,  $J_b$ , is shown as a solid line and that without  $J_b$  is shown as a dashed line. The dash-dotted line is the result of Cordey et al. [15] by the 2-dimensional velocity space calculation and the nonlinear treatment in e-e collision operator

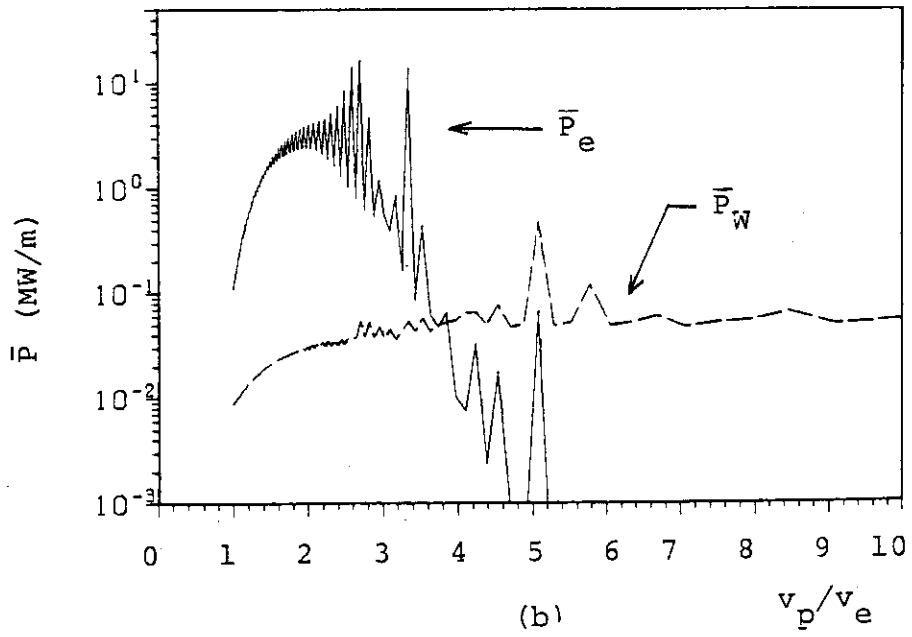
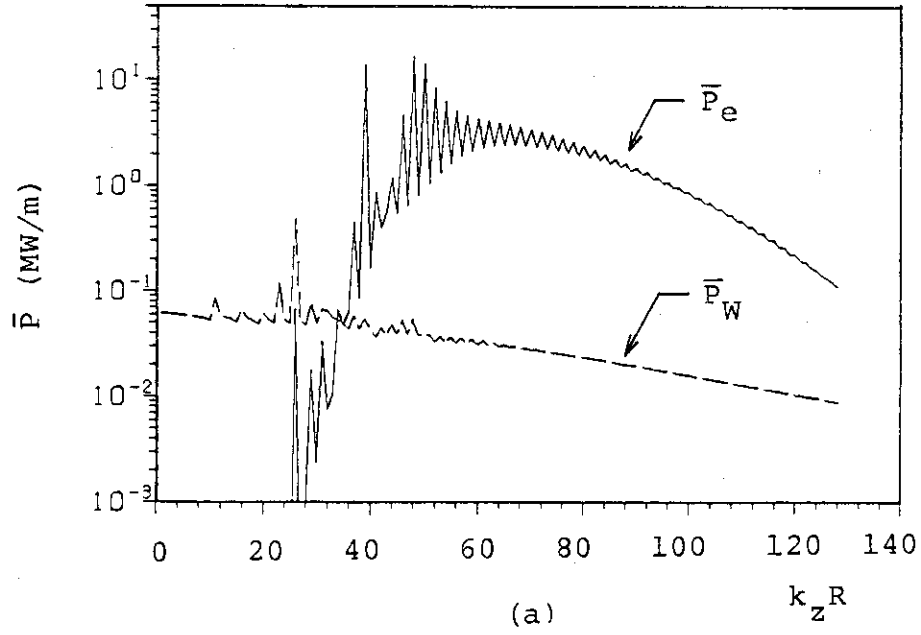


Fig.2 Absorbed power spectrum of electrons,  $\bar{P}_e$ , (solid line) and wall loss,  $\bar{P}_w$ , (dashed line) as a function of (a)  $k_z R$  and (b)  $v_p/v_e$  in the case of  $T_{e0}=30\text{keV}$  and  $n_{e0}=10^{20}\text{m}^{-3}$

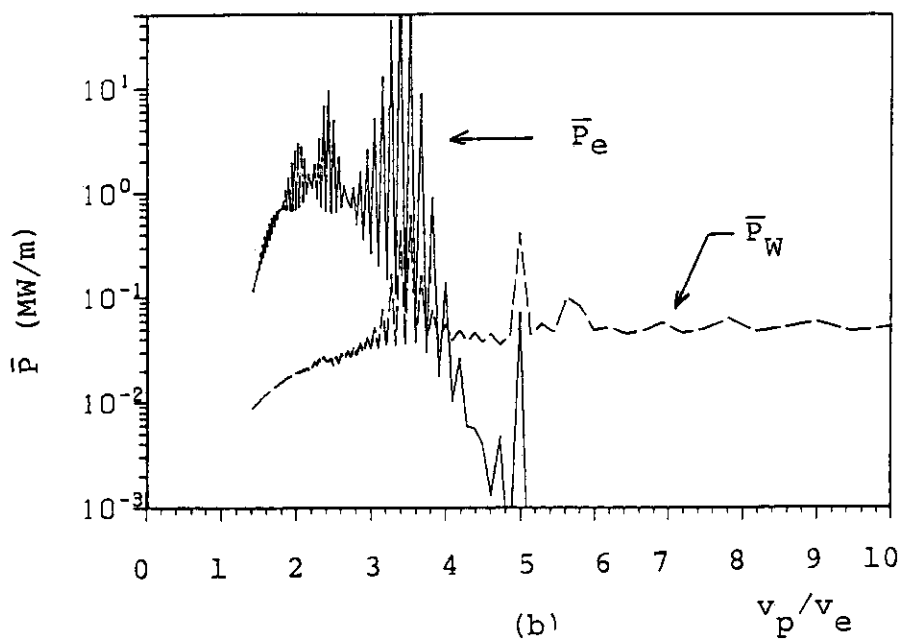
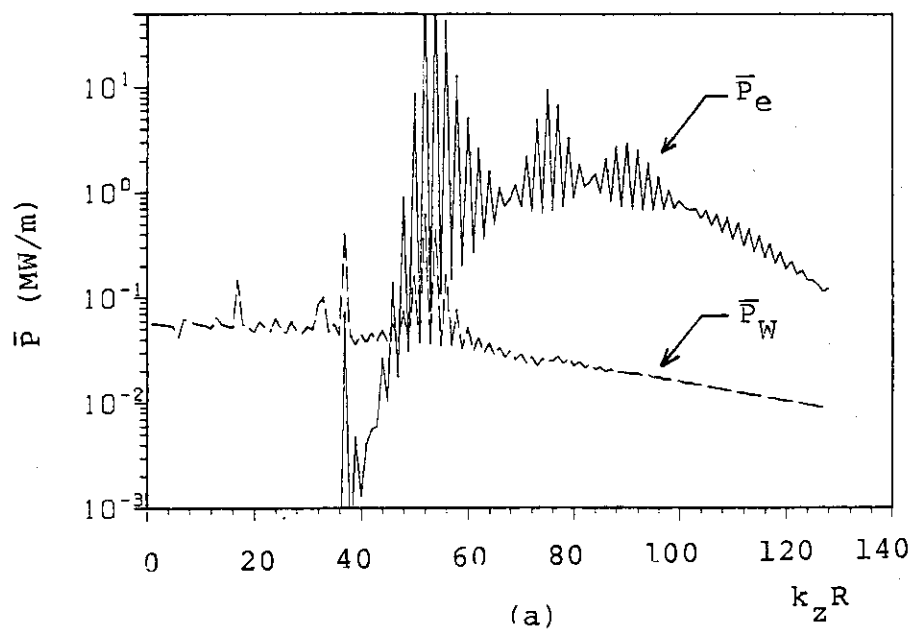


Fig.3 Absorbed power spectrum of electrons,  $\bar{P}_e$ , (solid line) and wall loss,  $\bar{P}_w$ , (dashed line) as a function of (a)  $k_z R$  and (b)  $v_p/v_{e0}$  in the case of  $T_{e0}=15\text{keV}$  and  $n_{e0}=10^{20}\text{m}^{-3}$

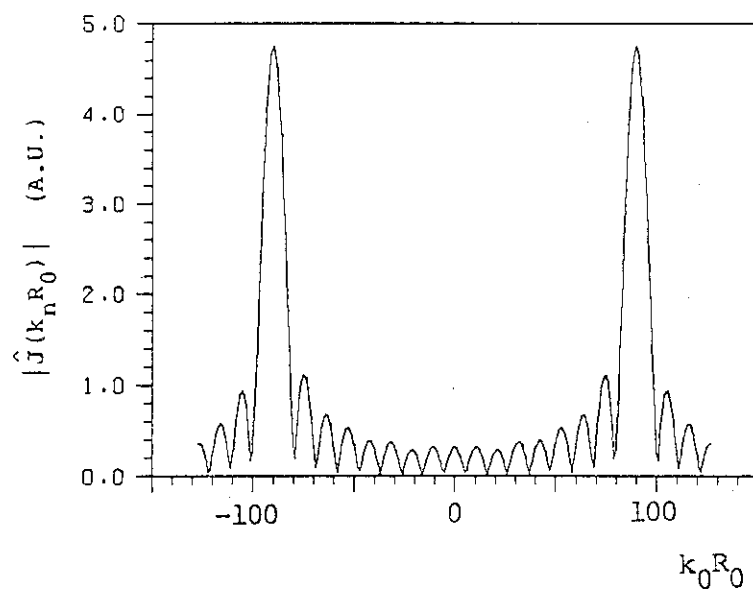


Fig.4 Spectrum of the antenna current in the case of  $N=17$ ,  $\Delta z=0.17\text{m}$  and  $\Delta\tilde{\phi}=180^\circ$

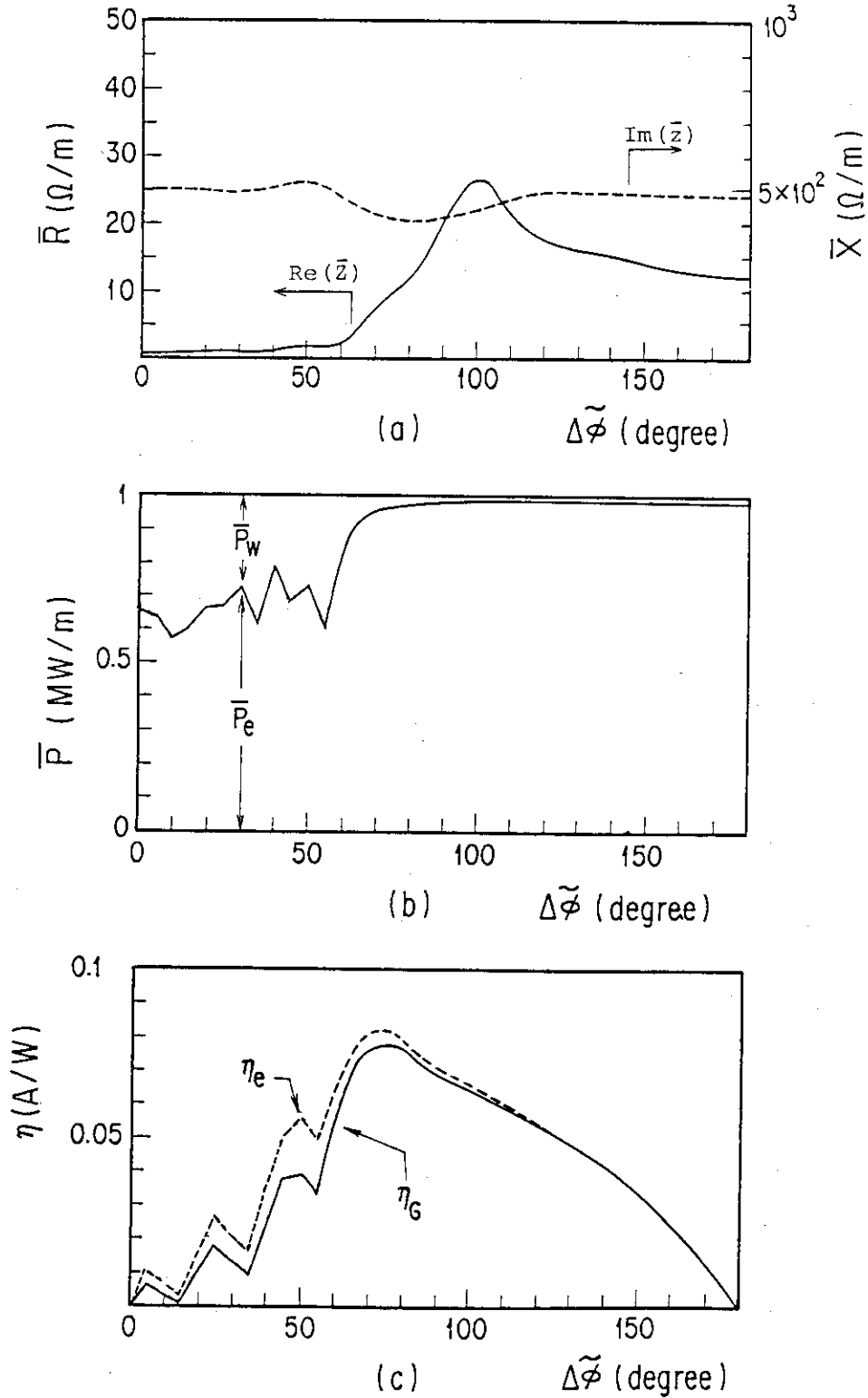


Fig.5 (a) Phase dependence of average loading resistance(solid line) and reactance(dashed line) per an antenna for plasma and antenna parameters listed in Table1  
 (b) Phase dependence of power absorbed by electrons,  $\bar{P}_e$ (solid line), and wall loss,  $\bar{P}_w$ ,(dashed line)  
 (c) Phase dependence of  $\eta_e$ (dashed line) and  $\eta_G$ (solid line)

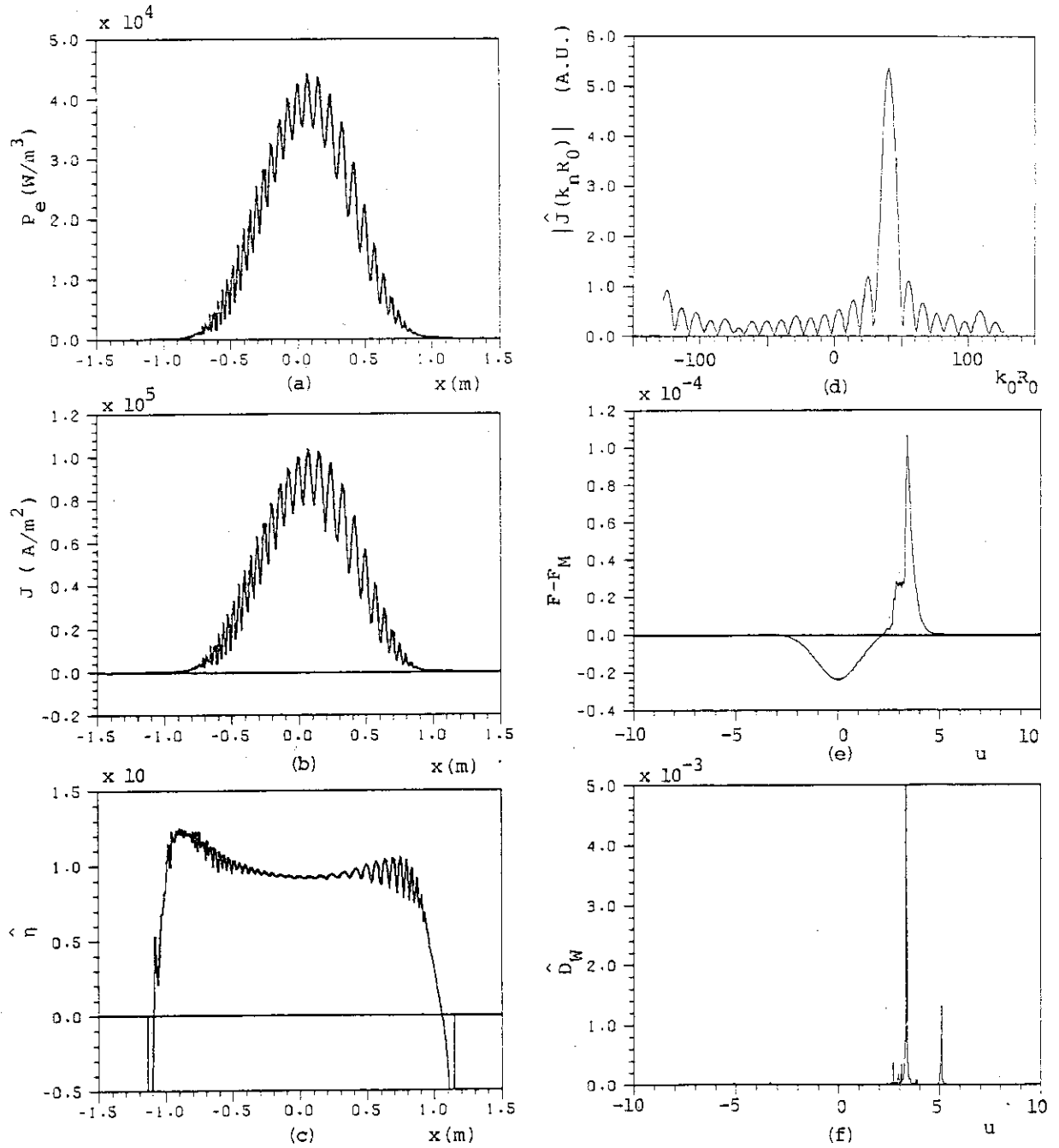


Fig.6 (a) Spatial structure of power density absorbed by electrons,  $P_e(x)$ , for  $\Delta\phi=80^\circ$ . Other parameters are the same as Fig.5  
 (b) Spatial structure of induced current density,  $J(x)$   
 (c) Spatial structure of normalized current-drive efficiency,  $\eta(x)$   
 (d) Spectrum of the antenna current,  $\hat{J}(k_n R)$   
 (e) Deviation of the parallel velocity distribution function of electrons from Maxwellian distribution,  $F(u)-F_M(u)$ , at the center ( $x=0$ )  
 (f) Normalized Diffusion coefficient,  $\hat{D}_W$

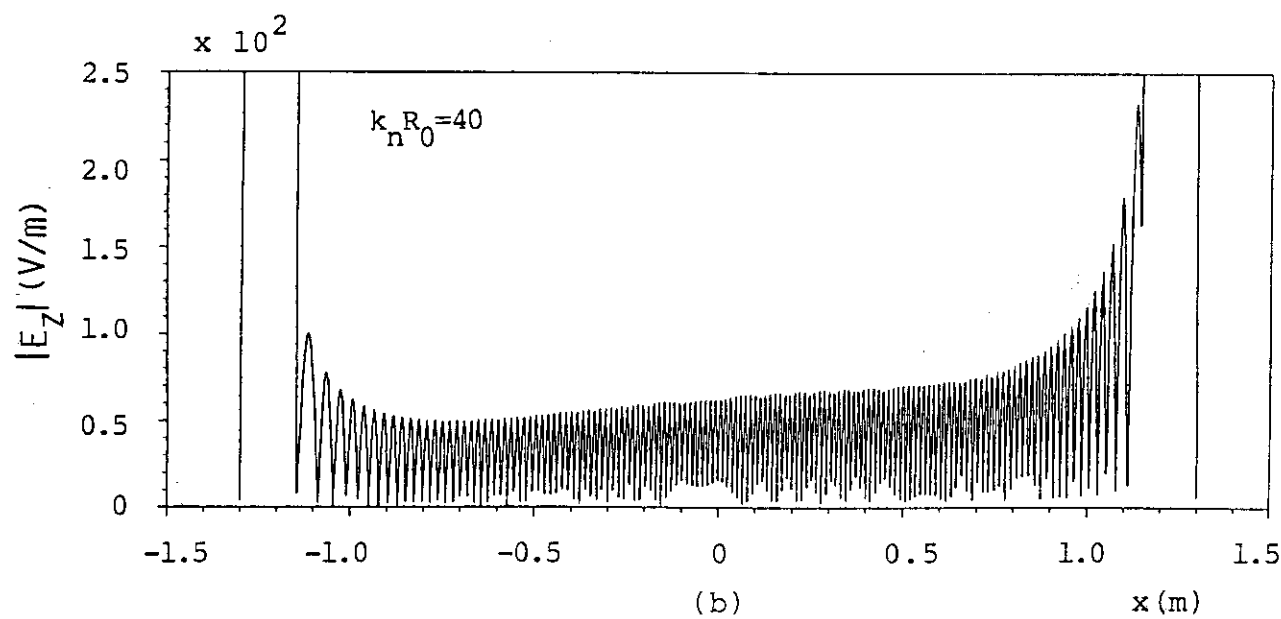
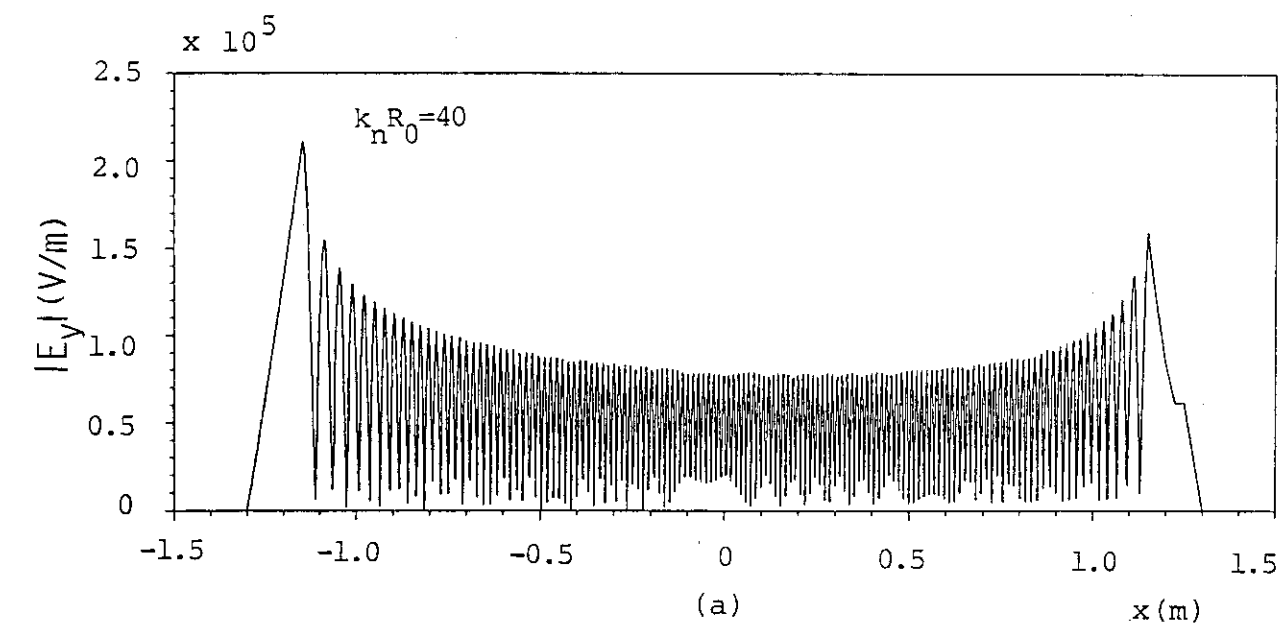


Fig.7 Spatial structure of Fourier component of the electric field,  
(a)  $|E_y(x)|$  and (b)  $|E_z(x)|$  for  $k_n R_0 = 40$  and  $\hat{J} = 1 \text{ kA}$

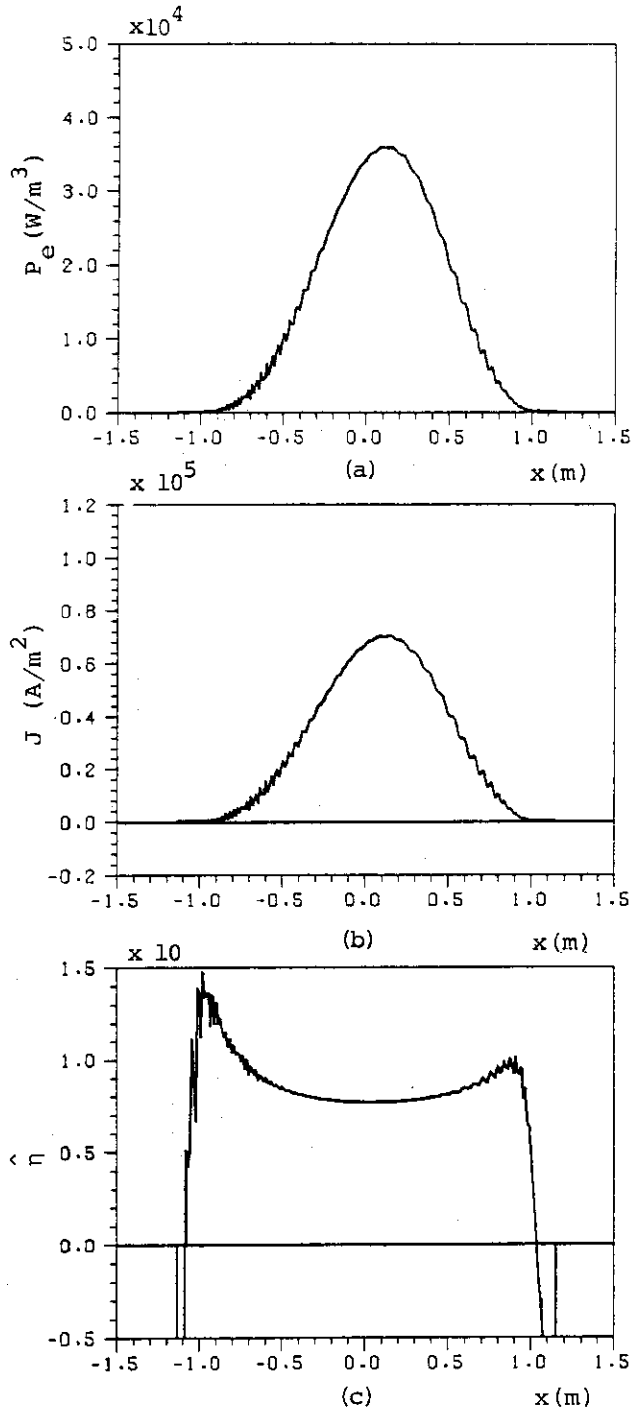


Fig. 8 Spatial structures of (a) power density absorbed by electrons,  $P_e(x)$ , (b) induced current density,  $J(x)$ , and (c) normalized current-drive efficiency,  $\hat{\eta}(x)$ , for  $\Delta\tilde{\phi}=100^\circ$

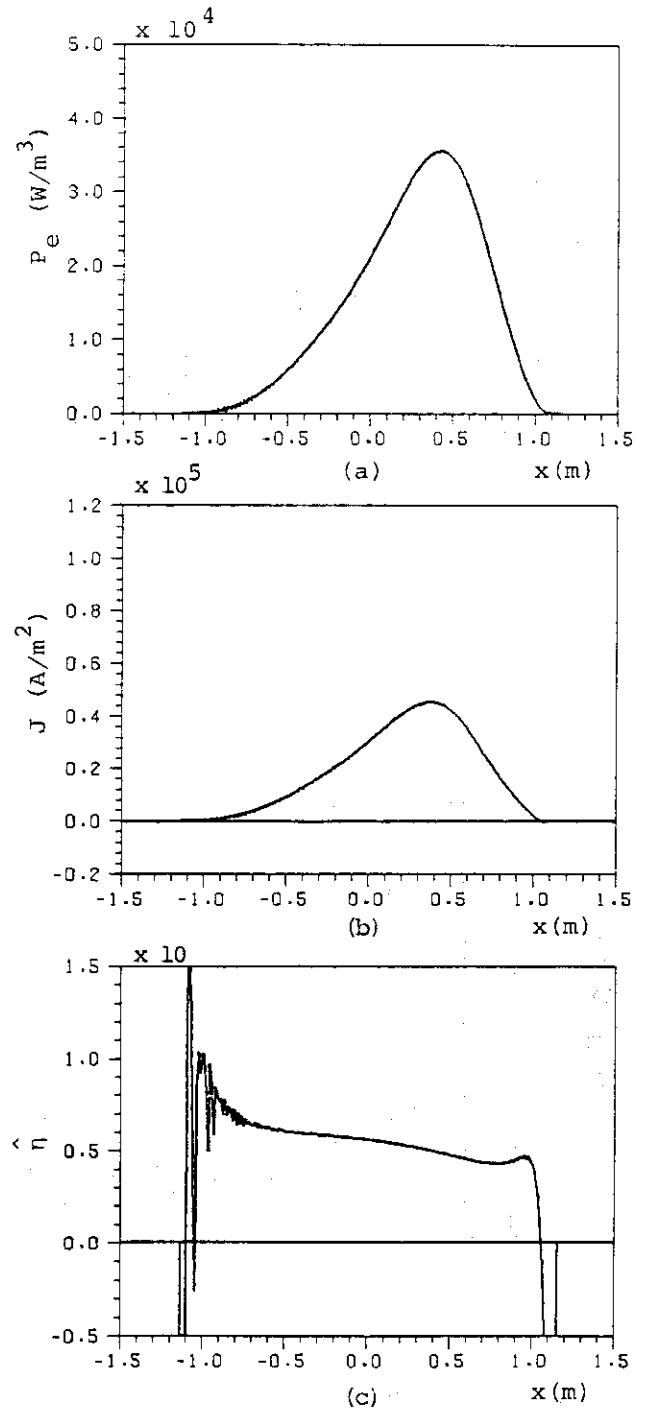


Fig. 9 Spatial structure of (a) power density absorbed by electrons,  $P_e(z)$ , (b) induced current density,  $J(x)$ , and (c) normalized current-drive efficiency,  $\hat{\eta}(x)$ , for  $\Delta\tilde{\phi}=140^\circ$



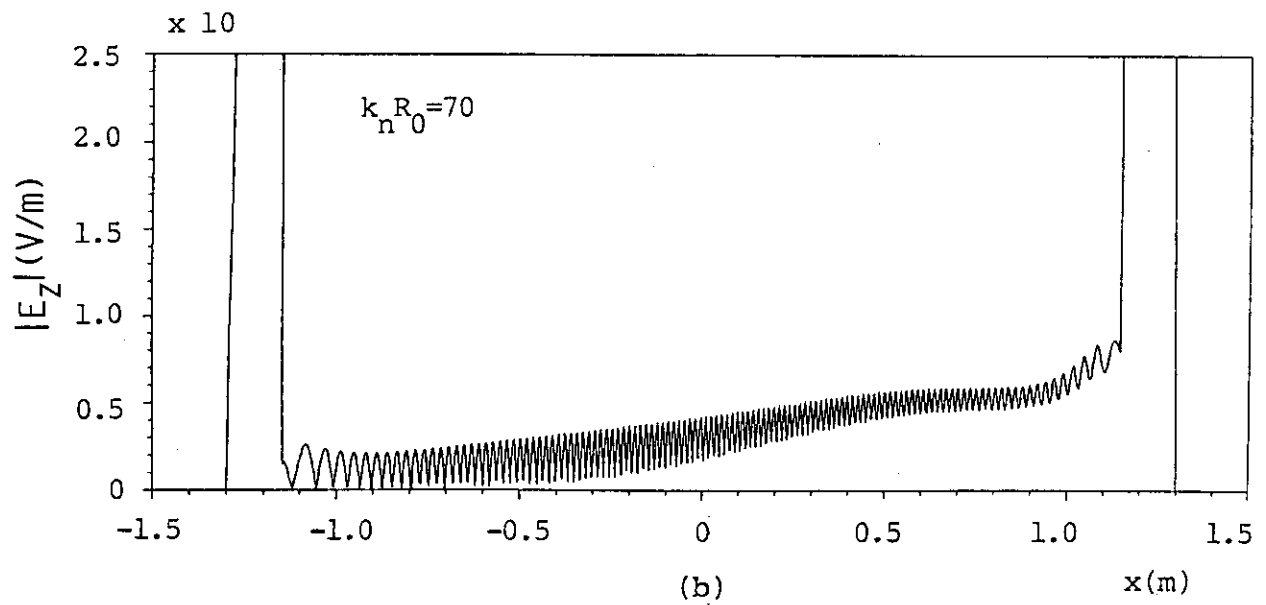
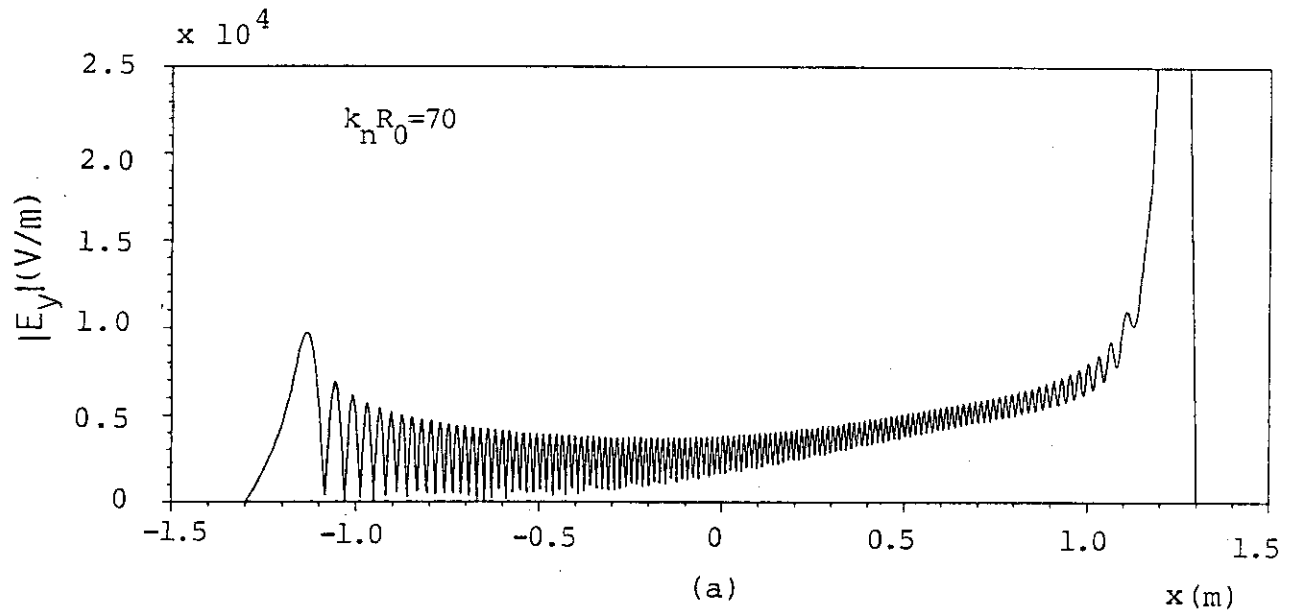


Fig.10 Spatial structure of Fourier component of the electric field, (a)  $|E_y(x)|$  and (b)  $|E_z(x)|$  for  $k_n R_0 = 70$  and  $\hat{J}(k_n) = 1 \text{ kA}$

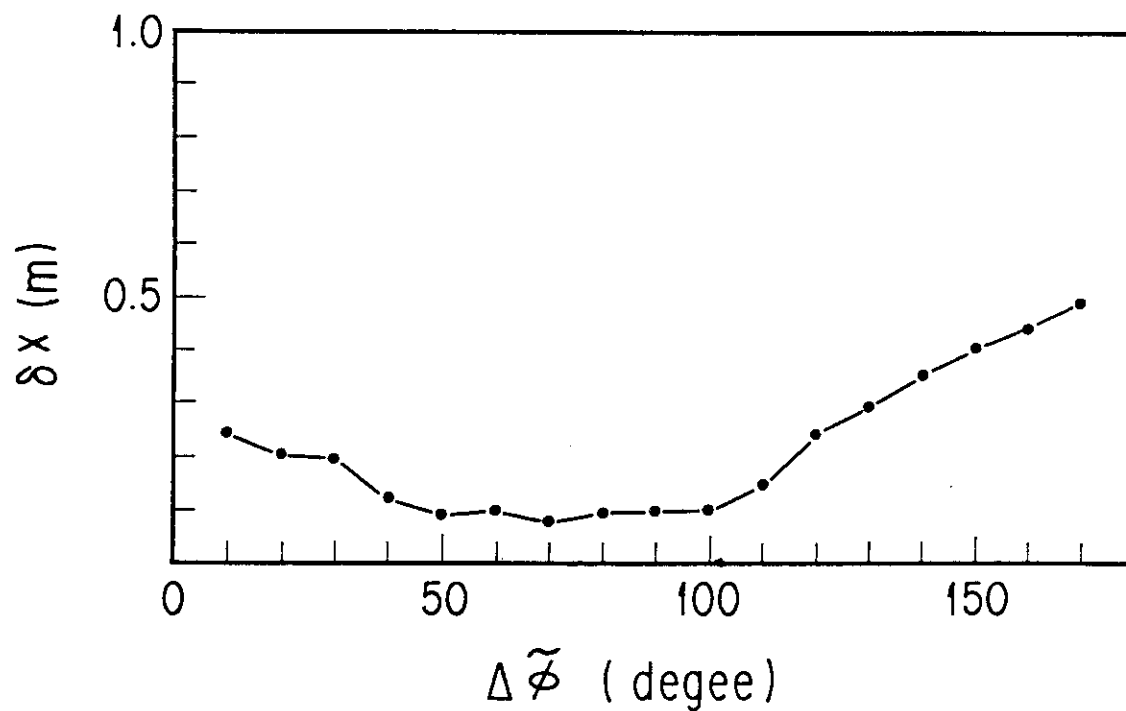


Fig.11 Deviation of the peak point of induced current density from the center( $x=0$ ) as a function of antenna phase difference  $\Delta \tilde{\phi}$

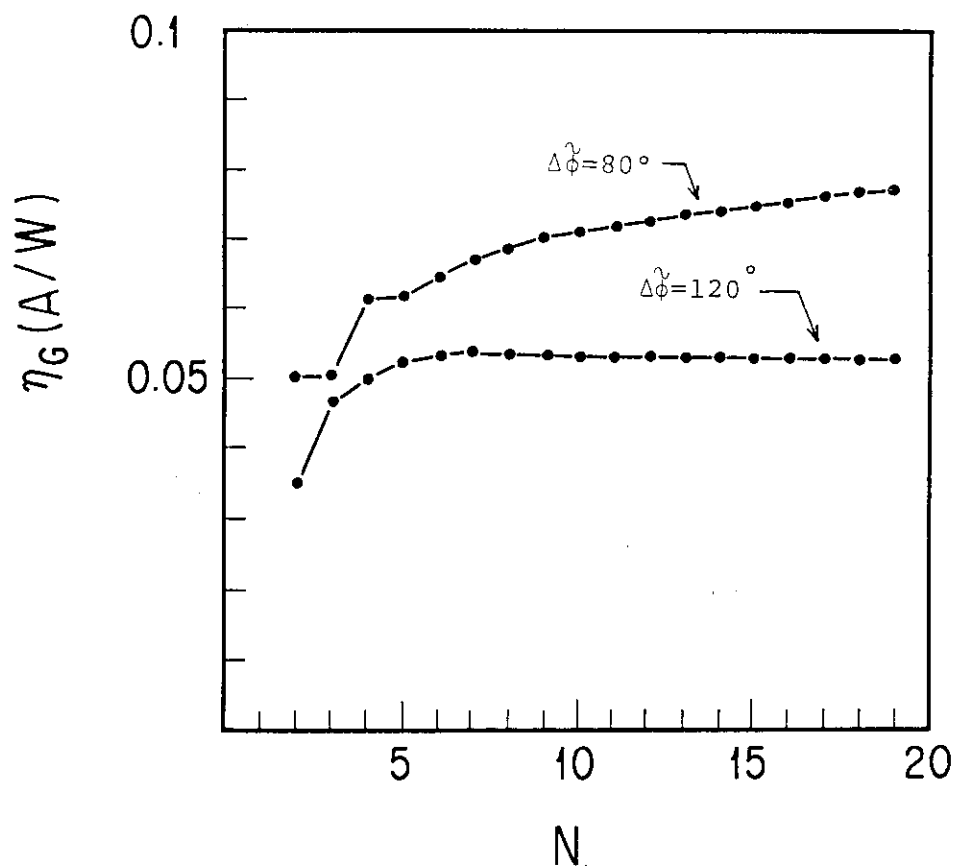


Fig.12 Dependence of  $\eta_G$  on total antenna number  $N$  in the case of  $\Delta \tilde{\phi} = 80^\circ$  and  $\Delta \tilde{\phi} = 120^\circ$ . Other parameters are the same as Fig.5

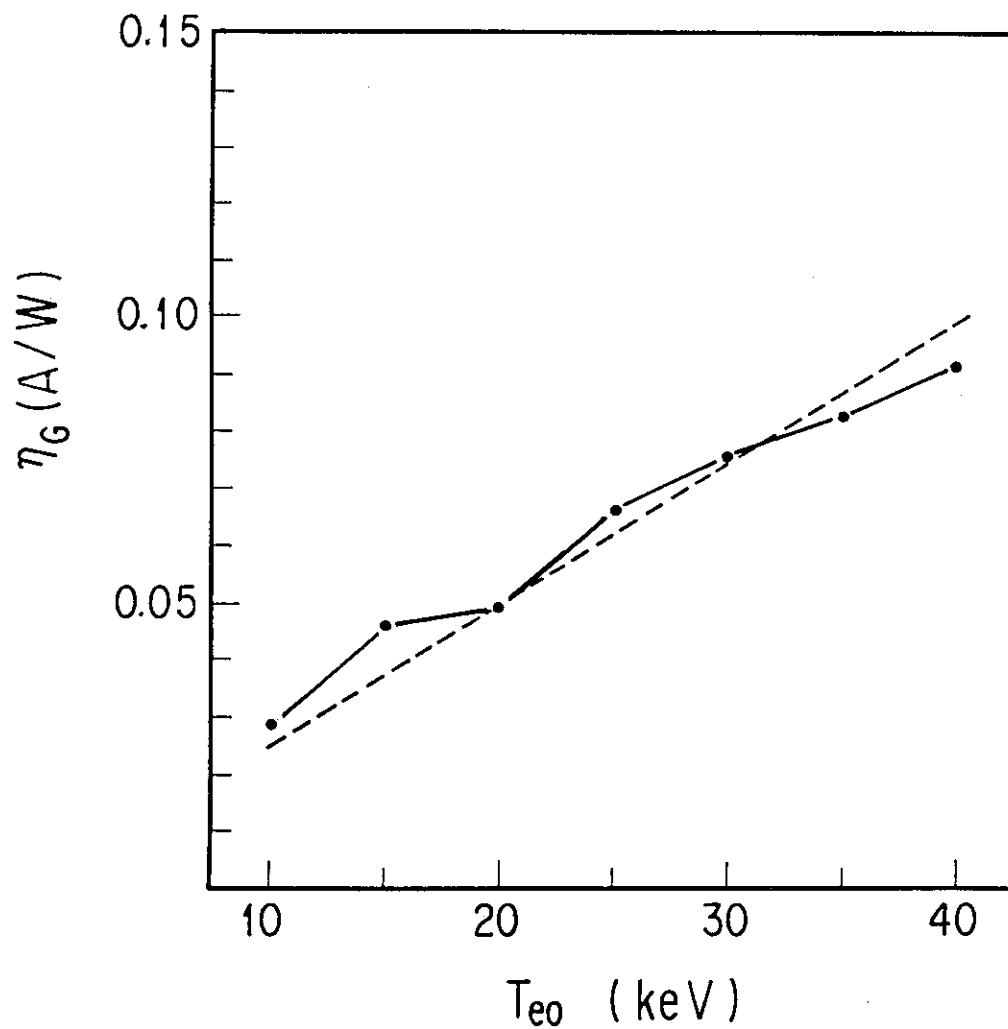


Fig.13 Temperature dependence of  $\eta_G$  for  $n_{e0}=10^{20}/\text{m}^3$ . The antenna phase difference is changed by the relation,  $\Delta\tilde{\phi}=80^\circ\sqrt{30/T_{e0}(\text{keV})}$  according to Eq.(28). The dashed line represents the fitting curve for  $\eta_G \propto 1/n_{e0}$

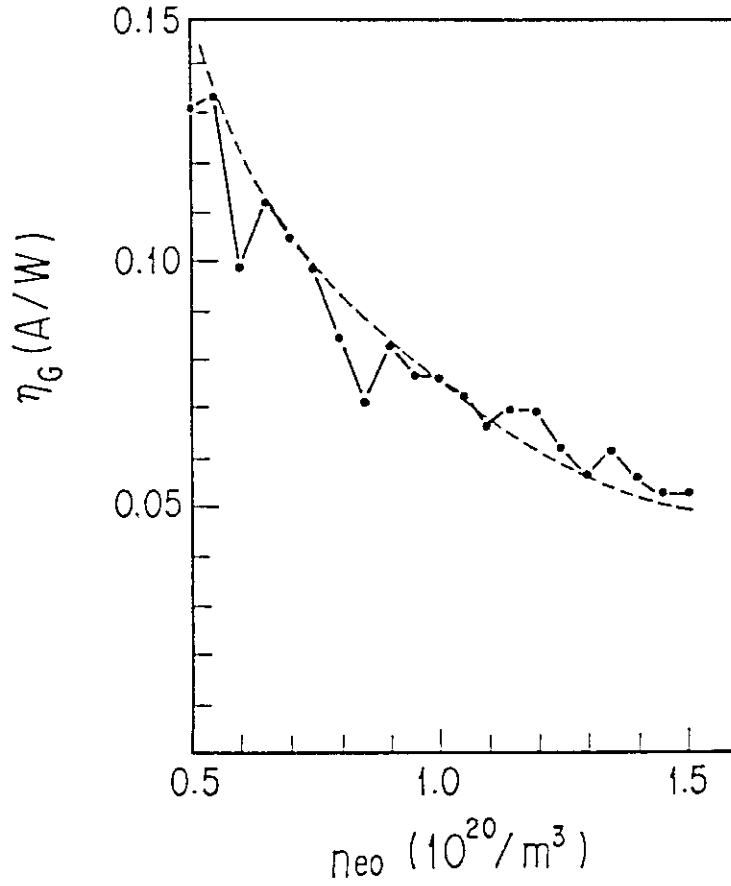


Fig.14 Density dependence of  $\eta_G$  for  $T_{e0}=15\text{keV}$  and  $\Delta\bar{\phi}=80^\circ$ . The dashed line represents the fitting curve for  $\eta_G \propto T_{e0}$

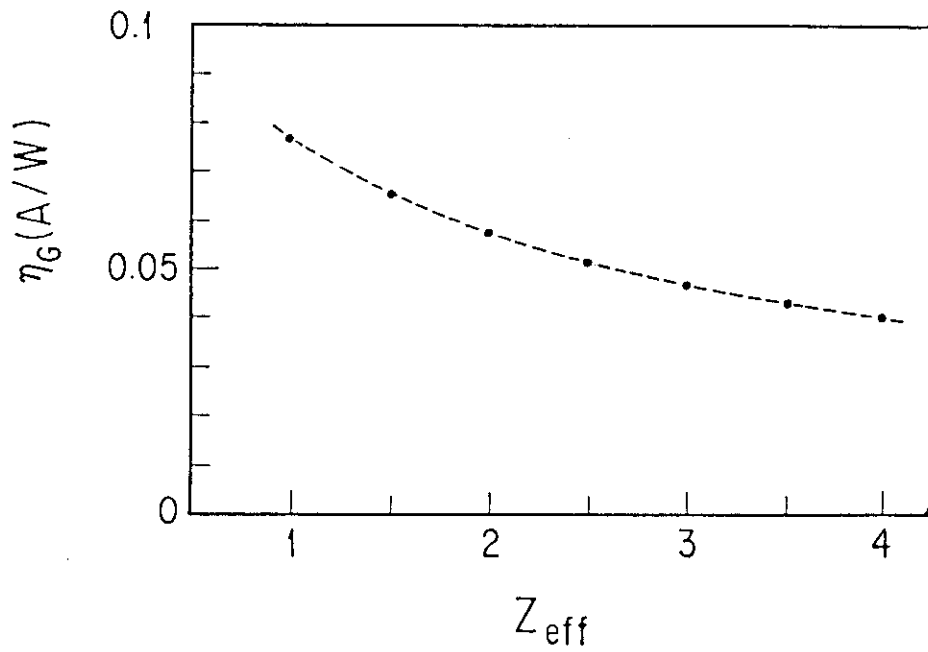


Fig.15 Dependence of  $\eta_G$  on the effective charge state  $Z_{\text{eff}}$ . Other parameters are the same as Fig.5